



TECHNISCHE
UNIVERSITÄT
WIEN
Vienna University of Technology

Diplomarbeit

CFD-Simulation of a high head Francis turbine and
comparison with experimental data

ausgeführt zum Zwecke der Erlangung des akademischen Grades eines

Diplomingenieur

unter der Leitung von

Dipl.-Ing. LENARCIC Markus

und

Univ.Prof. Dipl.-Ing. Dr.-Ing. BAUER Christian

E302 - Institut für Energietechnik und Thermodynamik

Eingereicht an der Technischen Universität Wien

Fakultät für Maschinenwesen und Betriebswissenschaften

von

Stefan J. Schoder

Matr. Nr. 0925762

Schubertplatz 4

3361, Aschbach Markt

schoder.jstefan@gmx.at

Vienna , February 11, 2015

Unterschrift



TECHNISCHE
UNIVERSITÄT
WIEN
Vienna University of Technology

Ich habe zur Kenntnis genommen, dass ich zur Drucklegung meiner Arbeit unter der Bezeichnung

Diplomarbeit

nur mit Bewilligung der Prüfungskommission berechtigt bin.

Ich erkläre weiters Eides statt, dass ich meine Diplomarbeit nach den anerkannten Grundsätzen für wissenschaftliche Abhandlungen selbstständig ausgeführt habe und alle verwendeten Hilfsmittel, insbesondere die zugrunde gelegte Literatur, genannt habe.

Weiters erkläre ich, dass ich dieses Diplomarbeitsthema bisher weder im In- noch Ausland (einer Beurteilerin/einen Beurteiler zur Begutachtung) in irgendeiner Form als Prüfungsarbeit vorgelegt habe und dass diese Arbeit mit der vom Begutachter beurteilten Arbeit übereinstimmt.

Vienna , February 11, 2015

Unterschrift

S. J. Schoder

Acknowledgement

Mein Dank gilt Univ. Prof. Dipl.-Ing. Dr.-Ing. BAUER an dessen Institut ich diese Arbeit anfertigte. Besonderer Dank gebührt Dipl.-Ing. Markus LENARCIC und Dipl.-Ing. Markus EICHHORN für die fachliche kompetente Betreuung, die umfassende Hilfe beim Vernetzen und die rege Diskussion.

Ein großes Dankeschön gilt meiner Freundin Barbara LAMPESBERGER, meinen Eltern (Michaela und Johann) und Geschwistern (Liesa Maria, Maria-Sophie, Joahannes Michael und Gregor Benedikt SCHODER), die mich während des Studiums hervorragend unterstützten.

Ein besonderes Dankeschön möchte ich meinen Freunden (David HALBMAYER, Andreas RUTHMEIER und Danny KLAS) aussprechen, welche immer mit Rat und Tat beiseite standen und für jede Diskussion ein offenes Ohr haben.

Abstract

This work investigates the turbulent flow in the high head Francis turbine of the Tokke model. The geometry and measurement data of the herein considered Tokke scaled down model are published on the Francis 99 workshop homepage [1]. Based on this data steady-state and unsteady flow simulations are set up in *commercial code* and unsteady flow simulations are set up in *OpenFOAM* at the BEP (best efficiency point) condition.

The whole domain is meshed in *Ansys ICEM CFD* using a block structured grid and grid refinement towards the hydraulic smooth walls. The wall boundary layer is resolved by $y_{mean}^+ \sim 30$ and automatic wall functions. Turbulent flow behavior is modeled by applying the shear stress transport model, $k\omega$ -SST. The grid convergence method verifies the ability of monotonic convergence. All further computations are based on this grid type meeting computational efficiency and validity of the calculated quantities. In contrast to the one passage model setup of the grid error estimation, the further simulations are performed on the full turbine model with 5M cells.

Commercial code: The efficiency is predicted accurately in the BEP and HL (high load) condition in the steady-state and unsteady simulation, with a maximum total deviation of $\eta\% < 1.5\%$. In the PL (part load) regime no obvious trend emerges for the global quantities. The averaged static pressure at the probes is estimated in accordance with the literature [2], [3], [4]. The tendency of underpredicting the probes in the draft tube and overpredicting the pressure in the runner domain, holds for all operating conditions. The computed mean velocity profiles coincide for the steady-state and unsteady CFD (computational fluid dynamics) simulation. In PL the velocity is captured accurately, whereas in the two other operating points, local effects are predicted incorrectly. However, the simulation results are consistent with [4], [5]. The main features of the pressure fluctuations are captured in the vaneless space. The efficiency losses in the distributor and the draft tube are evaluated according to [6] in all three operating points.

OpenFoam: is not capable of predicting the global quantities compared to the experimental data and *commercial code*. The efficiency deviates by $\eta\% = -13.2\%$. However, the local static pressure data is estimated similar to *commercial code*.

Kurzfassung

In dieser Arbeit werden die turbulenten Strömungsverhältnisse in der Francis Modellturbine des Tokke Kraftwerks untersucht. Die Geometriedaten und experimentell ermittelte Daten des Tokke Modells wurden im Zuge des Francis 99 Workshops öffentlich zugänglich gemacht [1]. Basierend auf diesen Daten wurden stationäre und transiente Strömungssimulationen mit *Commercial Code* und eine vergleichende transiente Rechnung in *OpenFOAM* im Bestpunkt durchgeführt.

Das Rechengebiet wurde in *Ansys ICEM CFD* mit einem blockstrukturierten Gitter vernetzt. Zu den Gebietsübergängen und zur Wand hin ermöglicht eine strukturierte Netzverfeinerung eine angemessene Auflösung der physikalischen Phänomene. In Wandnähe wird eine erste Zellhöhe von $y_{mean}^+ \sim 30$ als angemessene Auflösung bewertet. Das $k\omega$ -SST Turbulenzmodell mit automatischen Wandfunktionen beschreibt das turbulente Verhalten im Fluid. Die durchgeführte Netzunabhängigkeitsstudie verifiziert die monotone Konvergenzeigenschaft der erstellten Netze. Das Netz mit mittlerer Feinheit aus dem Abschnitt der Netzunabhängigkeitsstudie wird für die weiteren Rechnungen herangezogen. Im Unterschied zur Netzunabhängigkeitsstudie wurde jedoch die ganze Turbine für alle weiteren Berechnungen betrachtet und nicht das vereinfachte Sektorenmodell.

Commercial Code: Sowohl die stationäre als auch die transiente Simulation konnte den hydraulischen Wirkungsgrad der Francis Turbine mit einer maximalen Abweichung von $\eta\% < 1.5\%$ im BEP und im HL gut abbilden. Die erfassten mittleren Druckdaten in den Messpunkten streuten ähnlich wie in einschlägiger Literatur [2], [3], [4]. Bei den simulierten Strömungsprofilen konnten keine dominierenden transienten Effekte ermittelt werden, da die stationäre Rechnung mit der transienten sehr gut übereinstimmt. Im Bereich zwischen Leitapparat und Laufrad wurden die Druckschwankungen mit ausreichender Genauigkeit vorhergesagt. Die Anteile der hydraulischen Verluste im Leitapparat und im Saugrohr stimmen sehr gut mit der verfügbaren Referenzliteratur[6] überein.

Im Gegensatz zum *Commercial Code* weichen die Ergebnisse der globalen Größen in ***OpenFoam*** stärker von den experimentellen Daten ab ($\eta\% = -13.2\%$). Jedoch weisen die Resultate der simulierten statischen Drücke in *OpenFoam* eine ähnliche Abweichungstendenz, wie die *Commercial Code* Ergebnisse auf.

Contents

1	Introduction	1
1.1	Problem outline	3
2	Theory	4
2.1	Hydro power - Francis Turbine	4
2.1.1	Power plants	4
2.1.2	Energy transformation	6
2.2	Computational fluid dynamics	11
2.2.1	Navier-Stokes equations	11
2.2.2	Reynolds averaged Navier-Stokes equations	13
2.2.3	Two equation turbulence models	14
2.2.4	Numerical schemes	17
2.3	Simulation theory	19
2.3.1	Natural process	19
2.3.2	Physical model	20
2.3.3	Simulation	21
2.3.4	Validation of the results	22
2.3.5	Grid convergence method	23
3	Test rig	24
4	Numerical setup	28
4.1	Numerical setup - Grid independence study	28
4.2	Grid independence study - steady-state simulation	32
4.3	Numerical setup - Steady-state simulation	35
4.4	Numerical setup - Unsteady simulation	38
4.4.1	Solver setup - <i>Commercial code</i>	38
4.4.2	Solver setup - <i>OpenFoam</i>	39
5	Results	41
5.1	Integral quantities	41
5.2	Mean static pressure	43
5.3	Averaged velocity field in the draft tube	45

5.4	Pressure fluctuation	48
5.4.1	Pressure time domain	48
5.4.2	Pressure frequency domain	51
5.5	Flow energy losses	56
5.5.1	Distributor	56
5.5.2	Draft tube	58
6	Further investigations - Outlook	60
7	Conclusion	61
	Bibliography	I

List of Symbols

Abbreviation	Explanation
AMI	Arbitrary mesh interface
ASME	American society of mechanical engineers
BC	Boundary condition
BEP	Best efficiency point operation condition
CC	Curvature correction
CFD	Computational fluid dynamics
CFL	Courant Friedrich Lewy number
COM	Commercial code
DT	Draft tube
EXP	Experimental value
FFT	Fast Fourier transformation
FT	Fourier transformation
GCM	Grid convergence method
GGI	General grid interface
GV	Guide vane
HL	High load operation condition
KL	Kato Launder limiter
LDA	Laser Doppler anemometry
OP	Operation point
PDE	Partial differential equation
PL	Part load operation condition
RANS	Reynolds averaged Navier-Stokes equation
RN	Francis runner
RSI	Rotor stator interaction
RSM	Reynolds stress model
S	Steady-state simulation
SC	Spiral case
SST	Shear stress transport
SV	Stay vane
US	Unsteady simulation
Operators	
$(\cdot)_{,k}$	Partial derivative with respect to the k-th spatial coordinate
$(\cdot)_{,Dt}$	Material derivative

$(\cdot)_{,t}$	Partial derivative with respect to time
$\mathcal{F}(\cdot)$	Fourier transformation
$\overline{(\cdot)}$	Mean operator
Scales	
l_t	Turbulent length scale
y^+	Dimensionless wall distance
Special tensors	
δ_{ij}	Kronecker delta
e_{ij}	Strain rate tensor
s_{ij}	Deviatoric stress tensor
ϵ_{ijk}	Levi-Civita symbol, Permutation symbol
Σ_{ij}	Stress tensor
τ_{ij}^{Re}	Reynolds stress tensor
Symbols	
(r, θ, z)	Principal cylindrical coordinate directions
(x, y, z)	Principal Cartesian coordinate directions
α	Guide vane angle
β	Runner blade angle
Δt	Incremental time step
ϵ	Turbulent dissipation
η	(Hydraulic) Efficiency factor
\mathcal{A}	Boundary of the control volume
\mathcal{V}	Control volume
N	Total number of finite volume cells
μ	Dynamic viscosity
μ_t	Turbulent eddy viscosity
ν	Kinematic viscosity
ω	Specific turbulent dissipation
ω_r	Runner angular velocity
ρ	Fluid density
τ, t	Time
A	Vector potential
A_i	Faces of i-th finite volume cell
c	Velocity in an absolute coordinate system
C, σ	$k\epsilon$ model constants
c_τ	Wall shear velocity

D_h	Hydraulic diameter
D_r	Runner diameter
e_a	Approximated relative error
f	Volume force density
G	Physical quantity, grid convergence method
g	Gravitational constant
GCI	Grid convergence index
H	Net head
h	Representative grid size
I	Turbulent intensity
k	Turbulent kinetic energy
L	Angular momentum
n	Runner angular speed
N_p	Total sample size of the FFT data
P	Power
p	Static pressure
p_G	Order of the method estimated by the GCM
P_k	Production term of turbulent kinetic energy
Q	Flow rate, Discharge
R	Runner radius
$r_{i+1,i}$	Grid refinement factor of grid i
Re	Reynolds number
T	Torque
u	Velocity component due to the relative runner coordinate system
V_i	Volume of i -th finite volume cell
w	Velocity component in the relative runner coordinate system
Y	Net specific work

Units of physical quantities are based on the SI-unit system.

1 Introduction

For thirty years numerical fluid dynamics has been used to simulate hydraulic turbo-machines successfully [7]. In the early stages, problem-specific numerical code predicted simple estimations of flow fields. This first step led to powerful numerical simulation tools, having implemented a wide range of different numerical schemes and physical models. Recently simulation of multi-physics problems (one and two-way fluid structure interaction) and multi-phase flow are mostly investigated using the available numerical packages.

Simulation of fluid dynamics is known under the acronym CFD, computational fluid dynamics. Compared to simulations based on scaled down hydraulic turbo-machine models, CFD simulations are rather cost efficient and flexible. If one wants to perform an optimization of a turbine by testing prototypes, it will take quite a lot of time and money. Thus, virtual flow analysis is used to optimize the turbine shape in terms of the complex design criteria. The optimal design shape is then tested as a scaled down model. Measurements during that tests are again used to improve the numerical capabilities of the simulation software.

Recently hydro power plant operators compensate the volatile power supply of other green energy sources. Hydro power plants are fast power units providing frequency and voltage support, making them one of the essential grid units. Financially, providing grid stability is more beneficial, though mechanically the turbines are stressed due to fluid-dynamical sub-optimal loading conditions. Sub-optimal hydraulic loading conditions go in line with mechanical vibrations and intensely stressed material.

This complex environment of the power plant operators, as well as competition of the manufacturer, drives the development of CFD. The main geometrical quantities are fixed by the flow simulation, maintaining an optimal flow characteristic over a wide range of set points. As additional design criteria, material stress and dynamic excitation amplitudes shall be held within specified limits. The fluids physical conservation laws are the starting point of all further investigations. The CFD method describes the treatment of the conservation laws by temporal and spatial numerical discretization.

A robust simulation considers two important simulation feedback loops, namely verification and validation. Validation and verification of the code are essential to guarantee the accuracy of the outcomes with respect to the implemented equations. Commercially distributed software packages are generally verified and validated by the provider considering several test cases. Despite this, validation is part of the simulation to benchmark the physical model of the simulation as an accurate reference. This reference quantity can either be experimental data or outcomes of a higher instance model. High quality of the applied methods and errors are fixed via this final, essential simulation step.

Generally, a flow simulation contains several individual assignments. Initially, the desired geometry of the flow domain is assembled to generate the grid. Establishing a hexahedron block structured grid is one of the main workloads during a flow simulation. The quality of the grid shall fall within specified quality boundaries to ensure good convergence during the computation. Before the computation is started the initial physical state is defined and the numerical and physical models are chosen. After these pre-processing steps, the runnable model is started, and the solver processes the model. Finally, the generated output data is analyzed and the results are validated against measurements.

In recent years steady-state and unsteady flow simulation were performed on the Tokke scaled down model [8], [9]. During the Francis 99 workshop, steady-state investigations are performed using different solvers *commercial code* and *FOAM* as well as a various turbulence models in the three operating points [4]. Contemporary investigations predict flow phenomena in the BEP and HL accurately, though deviations occur in the PL regime. For this reason, this work addresses unsteady simulation and additional grid refinement towards a $y_{mean}^+ \sim 30$.

1.1 Problem outline

The practical part in *commercial code* covers the listed steady-state and unsteady flow simulations.

- A Grid convergence study based on Richardson extrapolation quantifies the numerical uncertainties due to uniform grid refinement. The model domain of this steady-state simulation is one passage of the turbine. Three different refinement stages are considered to evaluate the grid error. This error quantity supports the decision which of the three $y_{mean}^+ \sim 30$ grids is chosen for further simulations.
- Based on the chosen grid, steady-state single phase (water) simulations of the full Tokke model turbine are carried out. The three given operating points (PL, BEP and HL) are examined.
- In addition to the steady-state simulations, unsteady single phase simulations investigate the unsteady behavior of the Tokke model in the three operating points (PL, BEP and HL).

Since *OpenFOAM* is a cost free alternative flow simulation tool, the unsteady simulation capabilities of this software shall be investigated in this work.

- Thus, an unsteady single phase flow simulation of the full model is set up. In *OpenFOAM* only the BEP conditions are considered and integral quantities are evaluated.

2 Theory

The theoretical part of this thesis is motivated by the application of CFD in the field of hydraulic turbines. The fundamentals of Francis turbines are presented, including the application boundaries of such power plants and recent realizations. The concept of energy transformation is recapitulated and the necessary integral quantities (torque, head and efficiency) are derived. The second part includes a brief introduction to the computational and numerical methods used to model and solve the algebraic system of equations. The well known Navier-Stokes equations are interpreted, and two equation turbulence models are motivated to close the RANS equations with respect to the computational effort. Finally, a systematic simulation and validation framework is presented in the section simulation theory.

2.1 Hydro power - Francis Turbine

Hydro power is Austria's largest source of renewable electric energy [10]. The conventional potential is already well exploited in the whole country. The topology allows the three main hydraulic turbine types to be used in Austria: power plants with Kaplan-runners on the Danube and high head turbines (Francis and Pelton) in the Alps. In this work a scaled down model Francis turbine is considered. The corresponding full scale turbine is installed in the Tokke power plant in Norway.

2.1.1 Power plants

Francis turbine power plants are generally used for heads from 15m to 600m and medium discharge [11]. Today Francis runners are built with a maximum possible power transfer up to 800MW [12]. In the Tokke power plant, four Francis turbines with a total power of 430MW are installed, producing 2130GWh of annual electric energy. The power plant was built in 1961 and is supplied by a 17km long water piping system. [13]

Compared to the classical Tokke power plant, recent hydro power plants are often built as pump-storage power plant units. During excess energy production, the power plant is able to store electrical energy. Currently, storing water in a reservoir is the cheapest way to store electric energy. In 2011 the construction of the pump storage power plant Limberg II in Kaprun was completed. Ever since, two vertical Francis pump turbines with an installed power of 480MW and a discharge of $72\text{m}^3/\text{s}$ per turbine, have been supporting the electric grid in Austria. [14]

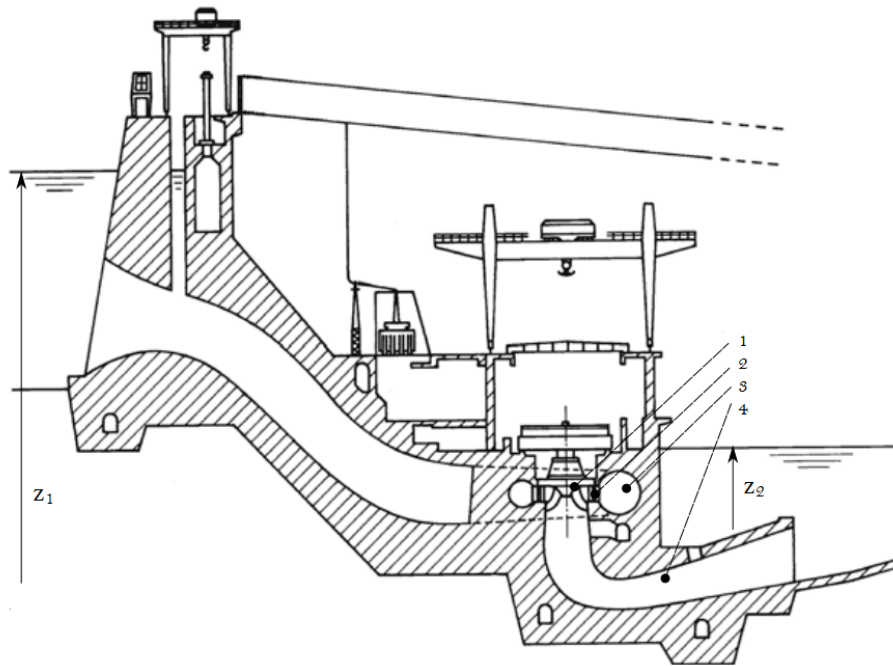


Figure 2.1: Francis power plant, (1) Francis runner, (2) distributor, (3) spiral casing and (4) elbow draft tube [15]

All Francis turbines consist of a spiral casing (3), a distributor (2), a runner (1) and a draft tube (4). These components are essential for an optimum performance of the power plant. The numbers of the components in this paragraph refer to figure 2.1.

Spiral casing The spiral casing links the pressure pipe of the power plant with the distributor of the turbine. The design of the spiral, redirects the flow from a linear flow to a swirled flow. The dimensions of the spiral casing are based on some restrictive assumptions. The flow leaving the spiral casing shall be axisymmetric and the pressure distribution nearly constant. Furthermore, the angular momentum at the interface shall be constant. With these constraints the spiral casing is designed with respect to a constant angular momentum (a nonlinear relationship links the cross-section and the angle) or constant fluid velocity in every spiral cross section (linear reduction of the cross section with respect to the

angle). Due to stability reasons, the spiral casings are often built with stay vanes. These vanes should not interfere for the flow passing through the spiral casing.

Guide vane Downstream the spiral casing, the distributor accelerates and applies the flow optimally towards the runner, considering the energy transformation process. The guide vanes are adaptable to the necessary operating points of the turbine. The guide vanes specified angular position, controls the incident angle of the flow into the runner passages and the discharge of the turbine by widening or reducing the distributors discharge area. As previously mentioned, the stay vanes of the spiral casing should not limit the distributor in its operational capability.

Francis runner The Francis runner is the core of the energy transformation process, but cannot act individually. The turbine's blades are connected by the hub at the top and by the shroud at the bottom. In the case of the Tokke power plant, the Francis runner has full length blades and splitter blades. Full length blades trap the flow in a channel from the turbine entry towards the exit. In the middle of every full blade passage, a splitter blade is located to regulate the velocity and pressure field in the runner's flow channels. The runner transforms the kinetic energy of the fluid flow into mechanical energy. A shaft connects the runner to the electric generator.

Draft tube The draft tube of the Francis turbine is located downstream the runner. Without a draft tube, the flow would exit the turbine with a spatial mean velocity in stream-wise direction c_{exit} . This exit velocity is not necessarily as low as the flow velocity of the river. Thus, a part of the kinetic energy is not transformed into mechanical energy by the turbine. To avoid this energy loss, a diffuser is added after the runner, which is called a draft tube. The draft tube decelerates the flow towards the river stream and recovers the otherwise lost energy. There are two restrictions to deceleration. The first, local pressure in the draft tube has to be higher than the vapor pressure of the medium to avoid cavitation. The second, the diffuser cone cannot be too steep so as to prevent flow separation.

2.1.2 Energy transformation

The energy transformation process represents the core purpose of the hydraulic turbo-machine. The available energy of the fluid stored in a reservoir is transformed into mechanical energy by the runner. The process efficiency determines

the main application ranges of most modern energy production devices and makes them economically and ecologically acceptable.

Available power The available energy of the stored fluid in the reservoir is quantified by the Bernoulli equation,

$$\frac{c^2}{2} + \frac{p}{\rho} + gz = \text{constant} \quad (1)$$

which represents the conservation of the specific energy. c describes the absolute velocity of the fluid, p the static pressure, ρ the fluid density, z the vertical coordinate with respect to a reference sea level and g the gravitational factor. After Bernoulli, the mass specific energy in the upper reservoir (subscript 1) is equal to the mass specific energy in the lower basin (subscript 2) and the transformed energy of the Francis runner Y .

$$\frac{c^2}{2} + \frac{p}{\rho} + gz_1 = \frac{c^2}{2} + \frac{p}{\rho} + gz_2 + Y \quad (2)$$

The physical quantities z_1 , z_2 are defined in figure 2.1. Since the ambient pressure acts on both water surfaces and the streaming velocity is equal to the river stream, these terms vanish which leads to

$$Y = g(z_1 - z_2) = gH \quad (3)$$

with the net head $H = z_1 - z_2$.

The total available power P_{av} of the streaming flow is

$$P_{av} = \rho Q Y = \rho Q g H \quad (4)$$

where ρ is the density and Q is the total discharge of the fluid. This is the maximum of transformable energy in the ideal case.

Velocity graphs Based on the turbine's main geometry, the absolute velocity in the turbine can be split in two components.

$$\mathbf{c} = \mathbf{u} + \mathbf{w} \quad (5)$$

The velocity component u in the rotating coordinate frame is represented as

$$u = \pi\omega_r D_r \quad (6)$$

with the runners rotational angular frequency ω_r and the runner diameter D_r . In difference to u the component w is measured relatively to the turbine coordinate system. Due to discharge, the meridian component of the absolute velocity c_m is fixed by the discharged cross-section $2\pi D_r l$.

$$c_m = \frac{Q}{2\pi D_r l} \quad (7)$$

The velocity components are illustrated at the runner inlet and outlet in figure 2.2.

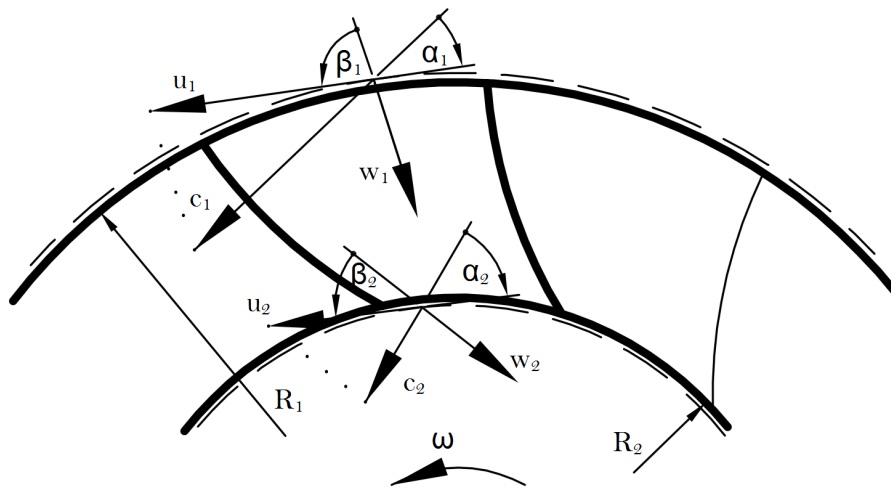


Figure 2.2: Definition of geometrical quantities and the velocity decomposition $\mathbf{c} = \mathbf{u} + \mathbf{w}$ in a Francis turbine [10]

In the three main different loading conditions (PL, BEP and HL), the absolute velocity's components develop differently. Figure 2.3 displays the velocity graphs of the Tokke turbine at the inlet side. The angles α and β , defined in figure 2.2, are marked in the velocity graph of the BEP in figure 2.3. The runner blade angle β is the same for all three operating points, since it is assumed that the flow follows the blade geometry smoothly.

The velocity graphs at the runners outlet side, are given in figure 2.4. In the BEP, the turbine is usually designed so that no angular momentum, which forms a swirl, leaves the turbine. This is not the case for the Tokke turbine. In PL and HL the direction of the swirl, relative to the runner's rotation, is estimated by the tangential velocity c_u . In PL the swirl rotates in the same direction as the runner. In the HL the swirl is counter-rotating.

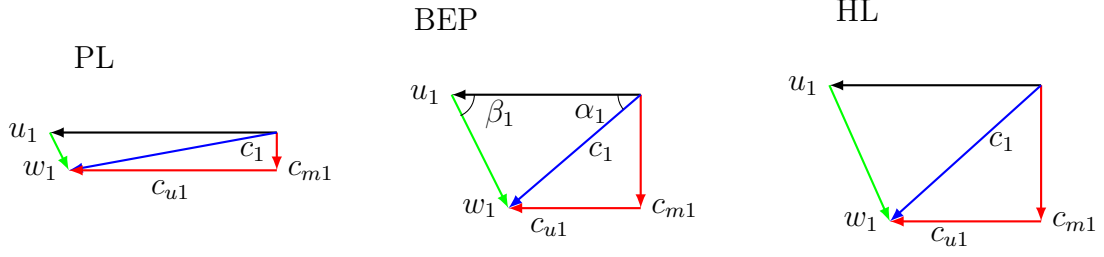


Figure 2.3: Velocity graphs at the Tokke runner inlet, $\mathbf{c} = \mathbf{u} + \mathbf{w}$, u in black, c in blue, w in green

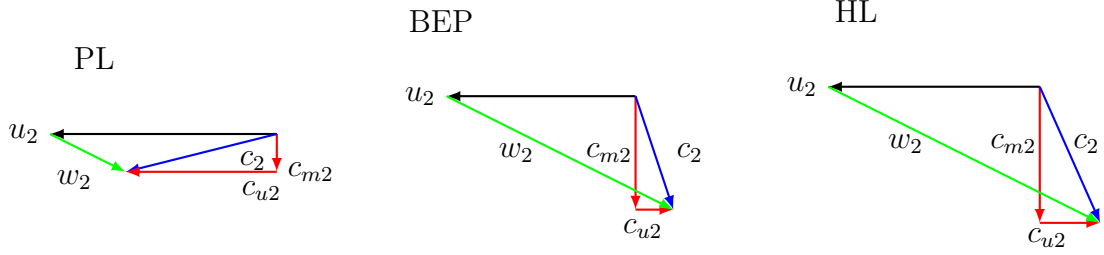


Figure 2.4: Velocity graphs at the Tokke runner outlet, $\mathbf{c} = \mathbf{u} + \mathbf{w}$, u in black, c in blue, w in green

These velocity graphs help to predict the power generated by the turbine. The derivation of the Euler turbine equation is outlined in the following and uses the conservation of angular momentum.

Euler turbine equation A rough estimation of the turbines torque is found by the Euler turbine equation, assuming steady-state flow conditions. Furthermore, gravity is neglected and it is assumed that the flow follows the blade geometry smoothly. The blades are considered to be infinitely thin and positioned throughout the whole runner, where all flow channels develop similarly throughout the runner.

The conservation of the angular momentum $L_i = \epsilon_{ijk} R_j p_k = \int_{\mathcal{V}(t)} \epsilon_{ijk} R_j c_k \rho dV$ in figure 2.2 yields to

$$L_{i,Dt} = \left[\int_{\mathcal{V}(t)} \epsilon_{ijk} R_j c_k \rho dV \right]_{,Dt} = \sum T_i \quad (8)$$

L represents the angular momentum, t the time, \mathcal{V} the control volume, ϵ_{ijk} the Levi-Civita symbol, R_j the runner radius and T the mechanical torque. Using the Reynolds transport theorem the conservation of momentum is written as

$$\int_{\mathcal{V}(t)} [\epsilon_{ijk} R_j c_k \rho dV]_{,t} + \int_{\mathcal{A}(t)} c_l \epsilon_{ijk} R_j c_k \rho dA_l = \sum T_i \quad (9)$$

Steady-state flow reduces the equation to the relevant boundary terms at the boundary \mathcal{A} .

$$\int_{\mathcal{A}(t)} c_1 \epsilon_{ijk} R_j c_k \rho dA_1 = \sum T_i \quad (10)$$

The velocity decomposition $c = u + w$ simplifies the cross product at the boundaries, leading to the Euler turbine equation. Thus, the torque transmitted to the runner shaft is estimated as

$$T_r = \rho Q (R_1 c_1 \cos \alpha_1 - R_2 c_2 \cos \alpha_2) \quad (11)$$

The geometrical properties and the definition of the relative velocity in the rotating coordinate frame as well as the absolute velocity are given in figure 2.2. Subscript 1 refers to the inlet and 2 to the outlet of the runners passage. [10]

Power generation and efficiency Using the torque, the power transmission P_t can be derived

$$P_t = T_r \omega_r = \rho Q (u_1 c_1 \cos \alpha_1 - u_2 c_2 \cos \alpha_2) \quad (12)$$

Since the Euler turbine equation incorporates no losses, an efficiency factor is introduced. Compared to the ideal assumption, the efficiency factor quantifies the occurring power dissipation. The main mechanical losses in a hydraulic turbomachine are:

- Hydraulic losses (Blade thickness, viscosity, turbulence, leakage, tribological losses)
- Mechanical losses (Vibration noise, losses in bearings and losses due to rotation in air and in the generator)

The efficiency factor η is defined as a ratio of the power output to the available power.

$$\eta = \frac{P_t}{P_{av}} = \frac{T_r \omega_r}{\rho g H Q} \quad (13)$$

2.2 Computational fluid dynamics

Computational fluid dynamics is a discipline merging analytic fluid mechanics and numerical mathematics with the purpose of deriving a general solving strategy for arbitrary flow phenomena. Regarding the practical part of the thesis, the fluid is assumed to be incompressible and Newtonian.

Using the conservation of mass and the Reynolds transport theorem the continuity equation is derived.

$$\rho_{,t} + (\rho c_i)_{,i} = 0 \quad (14)$$

The incompressibility assumption ($\rho_{,t} = 0$) simplifies the continuity equation 14 tremendously to 15. A constant temporal and spatial mass density imposes a divergence free flow field.

$$c_{i,i} = 0 \quad (15)$$

A divergence free flow field is also called solenoidal or incompressible, referring to the incompressibility assumption. Such fields can be expressed by a vector potential A as solenoidal part of the Helmholtz decomposition.

$$c_i = \epsilon_{ikl} A_{l,k} \quad (16)$$

These important simplifications even hold for compressible (more realistic) fluids at low temperature and low Mach-numbers (<0.3). The divergence free velocity field constraint simplifies the manipulation of the incompressible Navier-Stokes equations, with respect to two equation turbulence models.

2.2.1 Navier-Stokes equations

To derive the Navier-Stokes equation, the balance of linear momentum is applied to a physical domain, the control volume. The Reynolds transport theorem is applied to the control volume to quantify the change of linear momentum. According to Newton's law, this change is due to a volume force density f_i and surface forces $\Sigma_{ij}n_j$.

$$\int_{\mathcal{V}} [\rho c_i]_{,t} dV + \int_{\mathcal{A}} \rho c_i c_j dA_j = \int_{\mathcal{A}} \Sigma_{ij} dA_j + \int_{\mathcal{V}} [\rho f_i] dV \quad (17)$$

General rules of the material law theory fit the stress tensor Σ_{ij} to the following form for incompressible fluids [16]. The dynamic viscosity μ associates the shear stresses with the shear velocity rates in a linear manner. The Newtonian material law is expressed by this constitutive equation in three dimensions.

$$\Sigma_{ij} = -p\delta_{ij} + \mu(c_{i,j} + c_{j,i}) \quad (18)$$

All the diagonal elements of the stress tensor are normal stresses and the off diagonal components tangential stresses with respect to the surface. The divergence of the stress tensor is written as

$$\Sigma_{ij,i} = -p_{,i} + \mu(c_{i,jj}) \quad (19)$$

Applying the divergence integral theorem to the area integrals of the linear momentum balance 17, the boundary (area) integrals are transformed into a volume integral.

$$\int_{\mathcal{V}} [\rho c_{i,t} + \rho(c_i c_j)_{,j} + p_{,i} - \mu c_{i,jj} - \rho f_i] dV = 0 \quad (20)$$

Since the equation holds for arbitrary control volumes, the integrand has to vanish. This leads to the Navier-Stokes equations in the local strong formulation.

$$\rho c_{i,t} + \rho(c_i c_j)_{,j} = -p_{,j} + \mu c_{i,jj} + \rho f_i \quad (21)$$

The Navier-Stokes equation describes two structurally different flow phenomena laminar and turbulent flow. A limited range of length scales occurs during computation of a laminar flow, making it straightforward to compute. With increasing Reynolds number Re , the viscous forces are unable to keep the laminar layers together, hence turbulence mixing forming eddies occurs in the flow. These turbulent flow properties have a wide range of different length scales.

To simplify the resolution of all these eddy scales, two equation turbulence models are applied to close the Reynolds averaged Navier-Stokes equations (RANS). These models describe the turbulent quantities by two transport equations. The reason for using transport equations is due to the conformity with the conservation laws and the ability to use the same sort of solvers as for the Navier-Stokes equations.

2.2.2 Reynolds averaged Navier-Stokes equations

Turbulent flow is a chaotic fluctuating flow at high Reynolds numbers, described by the Navier-Stokes equations. However, the resolution of the different length and time scales of the existing eddies requires tremendous computational power. Thus, simplifications are made to model the computationally expensive equations by using adjusted transport equations. The equations predict the turbulent flow field in terms of mean quantities.

The turbulent flow field is assumed to follow a stochastic process evolving over the spatial and temporal domain. As in theory of stochastic quantities, the ergodic stochastic process can be split into a mean component and a fluctuating component. This decomposition is known in fluid dynamics as Reynolds decomposition

$$c(x, t) = \bar{c}(x) + c'(x, t) \quad (22)$$

Since the process is ergodic, the temporal, spatial and ensemble mean are equal for the flow field [17]. Thus, the two field properties are defined by the mean operator as

$$\bar{c}(x) := \lim_{\tau \rightarrow \infty} \frac{1}{2\tau} \int_{-\tau}^{\tau} c(x, t) dt \quad \overline{c'(x, t)} = 0 \quad (23)$$

The RANS are derived by applying the following mathematical manipulations: [18]

- Neglect the volume force density of the Navier-Stokes equations, without losing any generality.
- Insert the Reynolds decomposition into the Navier-Stokes equations and into the continuity equations.
- Take the mean operator over the whole equation.
- Use the continuity equation to simplify the RANS.

The obtained RANS equation is

$$\rho \bar{c}_{i,t} + \rho (\bar{c}_i \bar{c}_j + \overline{c'_i c'_j})_j = -\bar{p}_{,i} + \mu \bar{c}_{i,jj} \quad (24)$$

Since the Navier-Stokes equations couple the velocity and pressure field, a second equation system is found to describe the link to the pressure. The Poisson pressure

equation is derived by applying the divergence to the Navier-Stokes equations. Using the continuity equation for incompressible flow leads to

$$(\rho c_i c_j)_{,ji} = -p_{,ii} \quad (25)$$

the Poisson pressure equation.

These two coupled equations guarantee solvability of the velocity and pressure field.

The RANS equation characterizes turbulent flow, but differently to the laminar case it is not possible to solve it in terms of the mean quantities without additional knowledge. The occurring problem of too few equations is known as closure problem in literature.

The critical, but important difference to the laminar case are the correlations of the fluctuating velocity components, also known as Reynolds stresses τ_{ij}^{Re} .

$$\tau_{ij}^{Re} = -\rho \overline{c'_i c'_j} \quad (26)$$

Without this fluctuating quantities the mean flow Navier-Stokes equation is the same as in the laminar case. Therefore, the Reynolds stresses make a crucial difference.

One strategy is to model the Reynolds stresses by Boussinesq eddy viscosity hypotheses. The constitutive model is assumed in analogy to the Newtonian fluid.

$$\tau_{ij}^{Re} = 2\mu_t s_{ij} - \frac{2}{3}\rho k \delta_{ij} \quad (27)$$

μ_t is the turbulent dynamic viscosity and k the turbulent kinetic energy. Since the second term of the Boussinesq Reynolds stress model is incorporated in any offset pressure, only the deviatoric stresses s_{ij} have to be modeled by the closure equations. [19]

2.2.3 Two equation turbulence models

To close the Navier-Stokes equations computationally efficient, different turbulence models are proposed. The simplest models try to estimate turbulence by correlation considerations, more advanced schemes are based on averaged transport equations. Herein, two equation eddy viscosity models, are derived using the Navier-Stokes equations and Reynolds averaging. The denotation, two equation

eddy viscosity models, is based on the fact that two transport equations are used to predict the eddy viscosity.

The two additional quantities characterizing the flow are the turbulent kinetic energy k

$$k := \frac{1}{2} \overline{c'_i c'_i} \quad (28)$$

and the dissipation ϵ

$$\epsilon := \mu \overline{c'_{i,j} c'_{i,j}} = 2\mu \overline{e'_{ij} e'_{ij}} \quad (29)$$

with the strain rate tensor e_{ij} .

To derive the equation for the turbulent kinetic energy, the following steps are applied to the Navier-Stokes equations: [18]

- Multiply the Navier-Stokes equations by c_i and average the result.
- Multiply RANS by $\overline{c_i}$.
- Take the difference of both equations.
- Model the remaining transportation terms as $-\overline{c'_i p'} - \frac{1}{2} \overline{c'_i c'_j c'_i} \approx + \frac{\mu_t}{\sigma_k} \frac{\partial k}{\partial x_i}$.
- Model the production term as $-\overline{c'_i c'_j \frac{\partial \overline{c_i}}{\partial x_j}} = \tau_{ij}^{Re} \frac{\partial \overline{c_i}}{\partial x_j} \approx P_k$

After simplification, the k equation is found.

$$\rho k_{,Dt} = \frac{\partial}{\partial x_i} \left[\left(\mu + \frac{\mu_t}{\sigma_k} \right) \frac{\partial k}{\partial x_i} \right] + P_k - \rho \epsilon \quad (30)$$

The equation for the dissipation is derived by using the following steps:

- Subtract the RANS from the Navier-Stokes equation, so we get an equation for the fluctuating velocity component.
- Take the spatial derivative $(\cdot)_{,k}$ of the obtained equation, multiply the equation with $c_{i,j}$ and average the result over time.
- Multiply the equation by 2μ .
- Interpret the transportation, production and loss term as for the k equation, by simplified expressions.

The ϵ equation is obtained

$$\rho \epsilon_{,Dt} = \left[\left(\frac{\mu_t}{\sigma_\epsilon} + \mu \right) \epsilon_{,i} \right]_{,i} - C_{\epsilon 1} P_k \frac{\epsilon}{k} - C_{\epsilon 2} \rho \frac{\epsilon^2}{k} \quad (31)$$

The eddy viscosity is modeled by

$$\mu_t = C_\mu \rho \frac{k^2}{\epsilon} \quad (32)$$

The standard $k\epsilon$ model closure coefficients are $C_{\epsilon 1} = 1.44$, $C_{\epsilon 2} = 1.92$, $C_\mu = 0.09$, $\sigma_k = 1.0$ and $\sigma_\epsilon = 1.3$ [18].

Since the Reynolds stresses are assumed to be symmetric, errors occur at the walls. Hence, special wall treatment is required.

$k\omega$ and $k\omega$ -SST model Wall functions are needed in the $k\epsilon$ model to adapt the flow field to wall boundaries. To be able to apply the wall functions numerically, the first cells' dimensionless wall distance y^+ must be between 30 and 500 [20], so that the whole viscous sublayer is located in the first cell. Unlike the $k\epsilon$ model, the $k\omega$ model is capable of resolving the viscous sublayer. Thus, the grids y^+ value shall be very small (near to one). The $k\omega$ model uses a second transport equation for the specific turbulent dissipation ω , which is related to the $k\epsilon$ model.

$$\omega := \frac{\epsilon}{k} \quad (33)$$

Since the $k\omega$ model is sensitive to free stream values of the initial ω , Mentner proposed his $k\omega$ -SST model. The shear stress transport model (SST) uses the benefits of both models by introducing a switching function. This function gradually drives the model to the $k\omega$ or the $k\epsilon$ model where it is necessary. Furthermore, the turbulent viscosity accounts for the principal shear stress transport [21]. Often the SST model is implemented with automatic selection of the wall functions depending on the actual y^+ value.

$$y^+ := \frac{|c_\tau| y_{cell}}{\nu} \quad (34)$$

c_τ is the wall shear velocity, y_{cell} the height of the first cell at the wall and ν the kinematic viscosity.

Turbulent model parameters in CFD As for the velocity and pressure field, two additional initial and boundary conditions are set for the two turbulence modeling parameters. The turbulent intensity $I := \sqrt{\frac{3k}{2\bar{c}^2}}$ can be estimated in a long pipe flow by

$$I = 0.16Re_{D_h}^{-1/8} \quad (35)$$

with the Reynolds number Re considering the hydraulic diameter D_h [22].

The turbulent length scale l_t as [20]

$$l_t = 0.07D_h \quad (36)$$

Different gadgets in the piping system of the turbine (valves, rake) increase the turbulent intensity and length scales. Since this flow properties are difficult to measure, no robust estimation values are given for the turbulent model parameters.

2.2.4 Numerical schemes

The basic equations in fluid dynamics are well known balance equations conserving different continuous properties (mass, momentum, energy). These equations are represented locally by partial integral differential equations. The finite volume approach discretizes the spatial domain of the balance equation. The physical quantities are approximated with a desired polynomial of a specific order. Main fluid dynamic codes use first or second order schemes. The second area of algebraization takes place on the semi-infinite temporal domain. An implicit or explicit finite difference scheme approximates the time derivative of the balance. Due to stability purposes, time and spatial discretization have to be tuned accordingly.

Generally, CFD solvers work over two loops. The first loop steps forward in time. Whereas the second loop solves the nonlinear spatial problem iterative until the residues are sufficiently low. Both loops have to solve algebraic systems of equations.

Temporal discretization

Time dependent balance equations use implicit or explicit finite difference schemes to approximate the time derivative. The semi-infinite temporal domain is fitted by

different schemes of first or higher order (Euler, Crank Nicolson, Adam Bashford). Since the domain is semi-infinite, only initial conditions have to be set at time zero. This initialization can be rather simple or a more educated guess, e.g. a steady-state flow simulation field. A rule of thumb suggests to resolve a spatial rotation of one degree with the time discretization.

Spatial discretization

A generic balance equation consists of two main terms, the temporal change in the volume, which balances the second term and the surface discharges. These equations are represented locally by partial integral differential equations. The finite volume approach discretizes the spatial domain of the balance equation. The integral form of the balance equation is transformed by the divergence theorem. This lowers the order of spacial derivative and widens the functional space of the solution.

The basic steps deriving a finite volume method are applied to following equations:

$$u_{,t} + u_{,xx} + u_{,yy} = 0 \quad t \in [0, T] \quad \mathcal{V} \in ([0, 1] \times [0, 1]) \quad (37)$$

$$u(0, x, y) = 0 \quad (38)$$

$$u(t, 0, y) = u(t, 1, y) = u(t, x, 0) = u(t, x, 1) = 0 \quad (39)$$

- Similarly to other discretization methods, the finite volume method starts by integrating the partial differential equation over the whole domain and applying the divergence theorem.

$$\int_{\mathcal{V}} u_{,t} dV + \int_{\mathcal{A}} (u_{,x} dA_x + u_{,y} dA_y) = 0 \quad (40)$$

- The domain is split into sub-domains. In the center of each, a grid point is located, where the field variables are approximated.

$$\int_{V_i} u_{,t} dV + \int_{A_i} (u_{,x} dA_x + u_{,y} dA_y) = 0 \quad (41)$$

- The continuous field is approximated at three different mathematical levels.

- Quadrature of the integral:

$$\int_{V_i} dV = V_i \quad (42)$$

- Interpolation of the cell center values (full integer values) to the faces (half values):

$$u_{(i+1/2,j),x} = \frac{u_{(i+1,j)} - u_{(i,j)}}{x_{(i+1,j)} - x_{(i,j)}} \quad (43)$$

- Finite difference approximation of the time derivatives:

$$V_i \frac{u^{\tau+\Delta t} - u^\tau}{\Delta t} + \sum_{A_i} (u_{,x}^\tau dA_x + u_{,y}^\tau dA_y) = 0 \quad (44)$$

The incompressible Navier-Stokes equations are solved in the same way. The PDE (partial differential equation) is cast into a algebraic system of the velocity and pressure field. The two sets of coupled equations are then solved together.

2.3 Simulation theory

The simulation process consists of three main steps: modeling, solving and validation of the results. The modeling step suits the natural process into a physical model describing the phenomena. The physical problem is then transformed into a mathematical model. Usually there are no analytic solutions available in the case of nonlinear partial differential equations defined on complex boundaries. Hence, the model is solved numerically. In the simulation step, the numerical mathematical model is solved and the post processor provides modified output data. The final validation checks the model assumptions and ensures a high model quality. [23]

Figure 2.5 shows the principal steps during a simulation. This simulation process is not straight forward and has to be overcome in an iterative manner.

2.3.1 Natural process

The denotation natural process describes any transformation of states occurring in the real world. Often the processes cannot be observed directly, only inputs and outputs are measurable. The real world input and output data is used during the model validation, which is part of the simulation procedure. In the considered

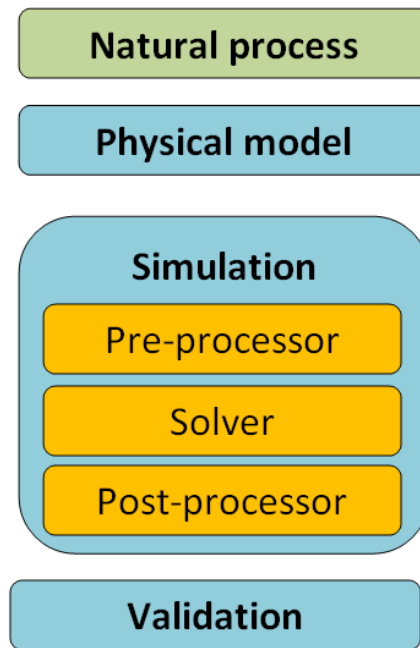


Figure 2.5: Generic simulation procedure, modeling a natural process in physics

simulation the natural process is the flow through the Francis turbine of the Tokke model.

2.3.2 Physical model

The physical model aims to represent the problem in terms of physical expressions, not necessarily as equations. From these laws and assumptions a mathematical model is derived. In experimental modeling a lot of tools are available to obtain models. Based on conservation laws and continuum theory, a classical way is chosen to express the physical model through partial differential equations. The conservation of mass is expressed by the continuity equation, whereas conservation of momentum is expressed by the Navier-Stokes equations. This coupled nonlinear boundary and initial value problem, challenges mathematicians all over the world. Fortunately, numerical solvers can cope with these types of problems. However, these mathematical models are based on assumptions, simplifying the natural process. With every assumption a particular part of reality is lost. So the results of the physical model deviate from experimental data systematically. If some model parameters are estimated experimentally, the model should not be over-fitted to something it cannot describe.

2.3.3 Simulation

The simulation procedure is the core step in solving the natural process. Numerical computation is used to solve the mathematically expensive equations, for which no analytic solutions are available. The main advantage of numerical code is its flexibility, coping with a lot of different mathematical problems and complex domains. The numerical simulation tools described herein, use a mesh-grid to simplify the domain shape. The simulation step consist of three sub-steps. Pre-processing starts with the generation of the computation domain and the grid. Following this, the user specifies the numerical set up of the computation and the output control procedure. The solver analyzes the pre-processed files and computes the desired results. In the final step, post processing, the solver output is modified taking into account the simulation objectives.

Pre-processor Pre-processing is the most time consuming and challenging part of numerical simulation. It starts with providing the relevant geometry of the model. The engineer decides the required extension of the computation domain by considering the relevant influences. With this geometry a grid is generated. Generally, two types of structurally different grids are worth considering. An unstructured grid is calculated automatically with medium mesh quality, but the invested time to mesh the domain is low. Alternatively, a block structured grid can be adapted with nearly no automation. After a first computation, a structured mesh refinement is performed to resolve physically interesting domains. Generally, the mesh grid shall be finer in the areas of huge gradients. During grid generation, grid quality parameters are considered to obtain a high quality grid.

The next step in pre-processing is the set up of the numeric model. First, initial values and the boundary values of the equations have to be set. The desired numerical schemes and the output values are defined during pre-processing. After the total model setup, a run check on the established model is carried out to determine basic simulation errors.

With the final simulation setup, a grid convergence study is performed to check the convergence capabilities of the set up.

Solver The model is solved on a server or any other computers with reasonable resources to perform a fast calculation of the problem. The solving processes have to be splittable to distribute them on a multi-core machine. This step requires computational power to interpret and solve the predefined human input.

The solver has to tackle initial value problems. This can be either processed implicitly or explicitly. Generally, implicit solvers are slower but more stable. Boundary values are incorporated in the solving procedure, which requires to solve a spatial algebraic system. The algebraic system of equations is obtained by discretizing the partial differential equations. The solver overcomes the problem in an iterative manner. Stepping one time interval into the future (first computational loop) and then evaluating the spacial algebraic system in an iterative manner (second computational loop) until it fulfills the applied convergence criteria.

The final process at each time step, or after a number of time steps, is to write the required results into the output files.

Post-processor After solving the model, output specific action is required to extract relevant data from the results. Here the resolution of physical interesting regions is judged. If it is too low the mesh is adapted adequately. The main post-processing outputs are tables of global and local variables, contour plots on surfaces and special model specific plots.

2.3.4 Validation of the results

The post processing provides and modifies the computational data to validate the results. The computed results are either validated against experimental data or against results of a more realistic model. During validation, two main checks are considered:

- Are the assumptions of the model valid?
- Is the established model capable of predicting the natural process?

The validation is the most important part of the whole simulation chain. It ensures a model that can reproduce the real world with a specific confidence.

Finally, do not confuse the term verification with validation:

- **Verification** is to check the correct implementation of the physical model as code. It ensures that the computation finds a solution to the physical model, not the real world problem.
- **Validation** is to check that the models assumptions hold and that the model has the same transformation behavior as the real process.

2.3.5 Grid convergence method

The uncertainty of the mesh is quantified by a grid convergence study. The convergence properties and the error of the computational grid are of main interest. Thus, one coarser and one finer grid are meshed. On the basis of these grids the uncertainty of the computational grid is quantified [24]. With this method the error of the solution is bound to a specific value expressed by the GCI (grid convergence index) of the extrapolated value. The extrapolation is based on Richardson extrapolation of the physical quantity G .

$$G_{\text{ext}} \approx G_1 + \frac{G_1 - G_2}{r^{p_G} - 1} \quad (45)$$

Furthermore, a procedure using three grids is able to verify the code's order of convergence [24].

To standardize the reporting of uncertainty, ASME (American society of mechanical engineers) [25] proposed a guideline of reporting uncertainty in fluid dynamics.

3 Test rig

The test rig, illustrated in figure 3.1, is a scaled down model of the Tokke power plant in Norway. Details about the Tokke power plant are given in the theoretical section 2.1.1. The corresponding model is located in Trondheim and the runner, as the core part of a hydraulic turbo-machine with a diameter of 0.349m, was designed at NTNU (Norges teknisk-naturvitenskapelige universitet). All measurements were carried out using the Tokke model in open loop mode. During measurement process, the control units ensured steady-state operating conditions. The test rig consists of a pressure vessel providing an equivalent pressure to 12 meters of water. A piping system links the pressure tank to the spiral casing. Seven long and seven short stay vanes stabilize the spiral casing mechanically. Coming through the spiral the water is applied to the runner by 28 adjustable guide vanes. The runner, consisting of 15 full length blades and 15 splitters, transfers the energy of the flow into electric energy via the generator. After the runner, the flow passes an elbow draft tube due to efficiency purposes and finally leaves the hydraulic turbo-machine to the downstream tank. The information provided in this section is based on the Francis 99 workshop webpage[1].

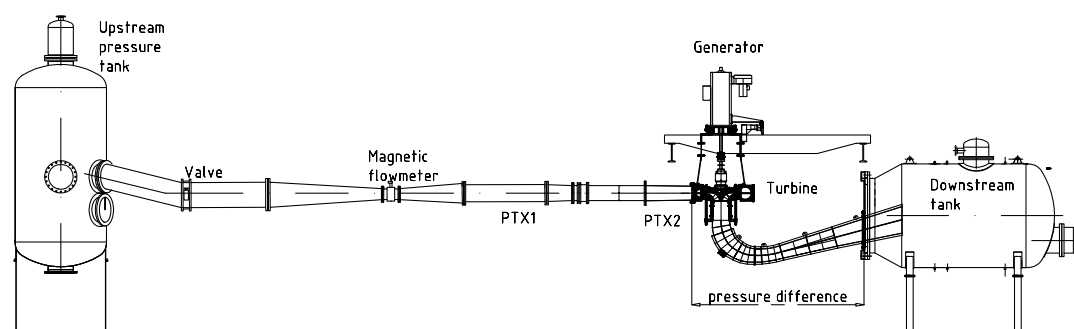


Figure 3.1: Tokke test rig at NTNU in open loop mode[1]

Geometry of the Tokke model

The geometry of the computational model is provided by the Francis 99 workshop and includes every physical part between the inlet of the spiral casing and the outlet of the draft tube. The turbine's shape is uniquely defined by 2D-drafts. The physically imposed structure of the simulation domain is illustrated in figure 3.2 with two separate stationary domains and a rotating domain.

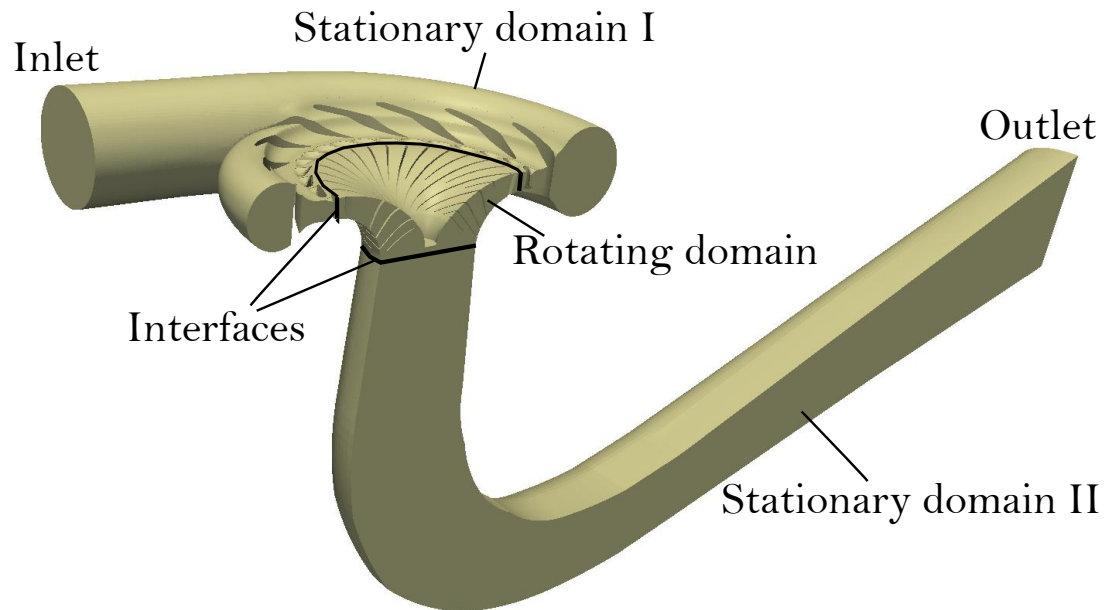


Figure 3.2: Structure of the hydraulic turbine model Tokke, provided by the Francis 99 workshop[1]

Operating conditions

Table 3.1 summarizes the presented operation conditions of the three operating points of the Tokke Francis turbine model. The quantities in the table are evaluated experimentally. The kinematic viscosity ν is $9.57 \cdot 10^{-7} \text{m}^2/\text{s}$ for all operating points. The gravitational constant g is $9.821 \text{m}/\text{s}^2$ in Trondheim.

Table 3.1: Operating conditions proposed for the Francis-99 workshop; Operating conditions for the LDA measurements (*) [4]

Objective	Unit	PL	BEP	HL	PL* _{LDA}	BEP* _{LDA}	HL* _{LDA}
H	m	12.290	11.910	11.840	12.290	12.77	12.61
Q	m ³ /s	0.071	0.203	0.221	0.071	0.21	0.23
n	1/s	6.770	5.590	6.160	6.770	5.74	6.34
α	deg	3.910	9.840	12.440	3.910	9.84	12.44
η_M	%	71.690	92.610	90.660	72.500	92.40	91.00
T	Nm	137.520	619.560	597.990	-	-	-
T_{fr}	Nm	6.540	8.850	7.630	-	-	-
Δp	kPa	120.394	114.978	114.033	-	-	-
p_{in}	kPa	219.930	216.540	210.010	-	-	-
ρ	kg/m ³	999.230	999.190	999.200	999.230	999.19	999.20

Experimental data

Measurements of fluid velocity and pressure are provided by the workshop to validate the CFD simulation against physics. Pressure sensor positions are summarized in table 3.2 and illustrated in figure 3.3. The abbreviations used in the table refer to the location in the corresponding figure.

Table 3.2: Cartesian coordinates of pressure sensors

Cart. Coord.	Unit	Pressure Sensors					
		VL01	S51	P42	P71	DT11	DT21
-	-	-	-	-	-	-	-
x	mm	262.3	-80.0	0.07	-66.6	-90.4	90.4
y	mm	193.5	83.8	179.40	42.3	156.6	-156.6
z	mm	-29.6	-50.9	-52.90	-86.0	-305.8	-305.8

The sensor VL01 is located in the vaneless space between the guide vanes and the runner blades. Sensors DT11 and DT21 are positioned near the wall in the draft tube entrance immediately after the runner outlet. P42 and P71 are two sensors measuring the static pressure on the pressure side of the runner's main blade. S51 is placed at the runner's blade suction side.

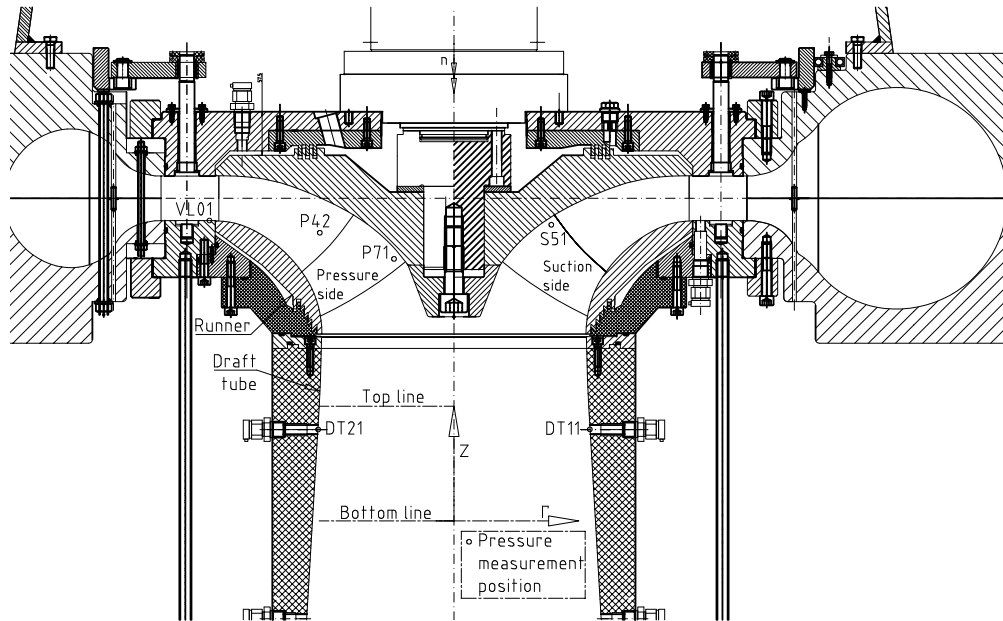


Figure 3.3: Pressure sensor positions[1]

The velocity measurements were carried out by Laser Doppler Anemometry (LDA) along two lines in the draft tube (figure 3.3 and table 3.3). The first line is located next to the runner draft tube interface and the second line further along the draft tube, but prior to the elbow. The origins of the two lines are given in table 3.2. In the best efficiency point and in the high load point, vibrations interfered the measurements. Thus, the operating conditions were changed consistently to the one of table 3.1. All columns with a LDA subscript display the current measurement conditions of the available velocity data.

Table 3.3: Cartesian coordinates of the LDA measurement points

Cart. Coord.	Unit	Top Line		Bottom Line	
		Start	End	Start	End
x	mm	0	-178.9	0	-196.5
y	mm	0	0	0	0
z	mm	-243.4	-243.4	-561.4	-561.4

Negative axial components of the velocity is towards the stream-wise direction in the draft tube and positive radial direction in the runner's rotational direction. Several LDA measurements were carried out along these lines for the three operating conditions and the data was provided via the workshops webpage.

4 Numerical setup

4.1 Numerical setup - Grid independence study

A grid convergence study, based on Richardson extrapolation, quantifies the numerical uncertainties due to uniform grid refinement. The domain of this steady-state simulation is one rotational periodic passage of the turbine model. The numerical error due to the discretization and the actual order of convergence, are evaluated by three uniform grid refinement stages. The blocking of the components was provided by [4].

Grid

The one passage model's inlet domain mesh is embedded in a simplified periodic slice of the geometry, with a pitch angle of $\pi/7$. Figure 4.1 shows the obtained final grid, with $y_{mean}^+ \sim 30$.

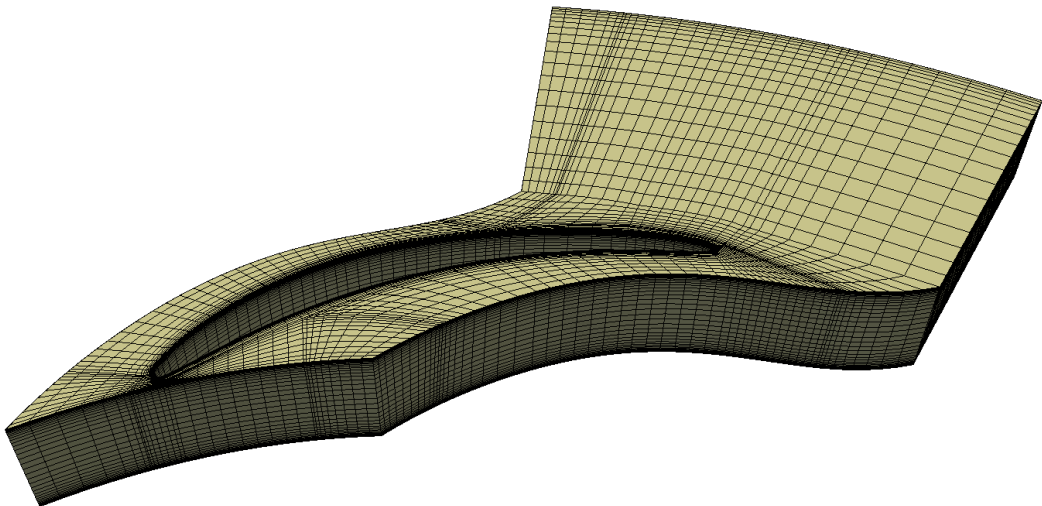


Figure 4.1: One passage model's inlets mesh grid structure $y_{mean}^+ \sim 30$

The guide vane mesh is seeded in one of the 28 passages. Figure 4.2 shows the obtained grid. The guide vane is meshed separately for all three operating points (PL, BEP, HL), with a slightly tilted guide vane.

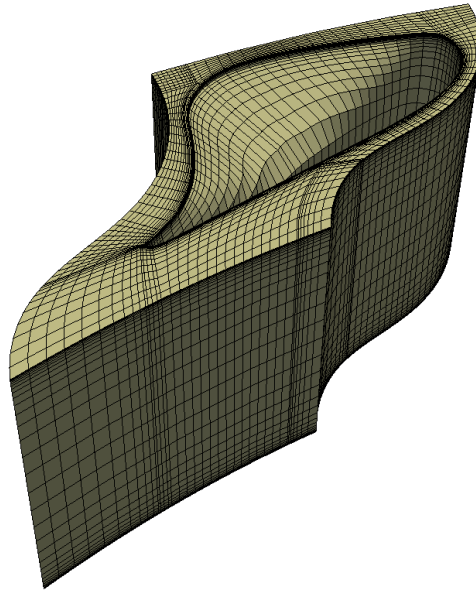


Figure 4.2: One passage model's guide vanes mesh grid structure $y_{mean}^+ \sim 30$

The runner's mesh of the one passage model is ingrained in a simplified periodic geometry, with a pitch angle of $2\pi/15$ (figure 4.3).

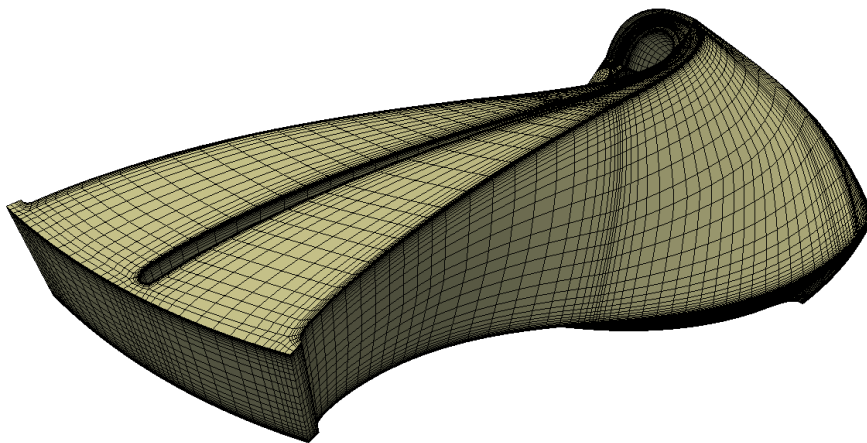


Figure 4.3: One passage model's runners mesh grid structure $y_{mean}^+ \sim 30$

The one passage model's mesh of the draft tube, is a block structured grid consist-

ing of 30 hexahedron blocks. Figure 4.4 shows the reference grid. The cells grow towards the draft tube outlet to minimize the total cell number.

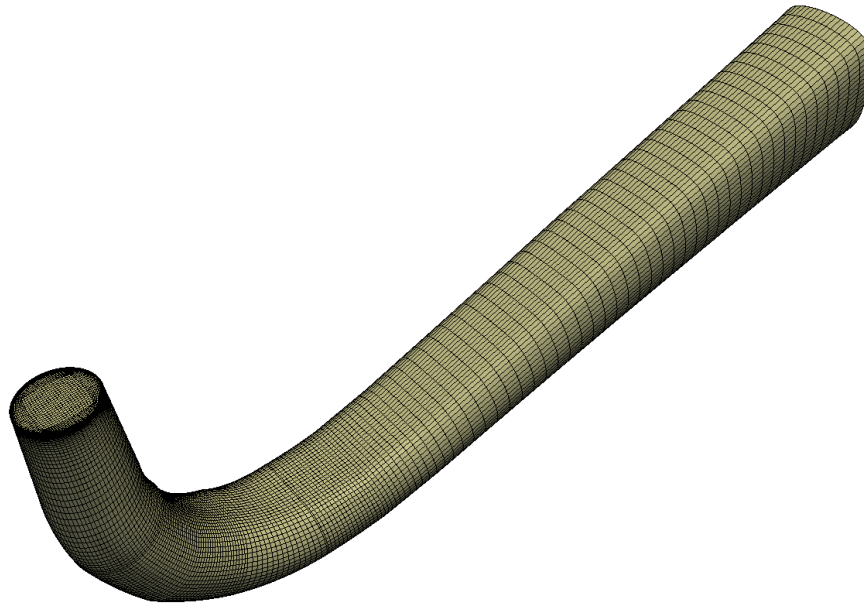


Figure 4.4: Grid structure $y_{mean}^+ \sim 30$ of the draft tube's mesh

Table 4.1: Summary of the one passage model's mesh grid with three uniform refinements

	coarse	medium (reference)	fine
Total Cells	213k	504k	1227k
Grid refinement factor	-	1.33	1.35
Determinant	>0.3	>0.22	>0.17
Angle	>12°	>12°	>11.7°
Refinement ratio	1.3	1.3	1.3

Solver setup

The grid convergence study is set up in *commercial code*. The flow domain (figure 4.5) is separated into the relevant sub-domains (stay vane inlet, guide vane, runner and draft tube). The solver domain and the rotor-stator interface are based on the findings in paper [4], where no significant differences occur between the model domain setup and the type of the rotor-stator interface. The fluid properties are chosen according to the operation point in table 3.1. The turbulence is modeled based on the RANS, which is closed by the two equation turbulence model $k\omega$ -SST, using automatic wall functions. A simple subsonic mass flow is applied at

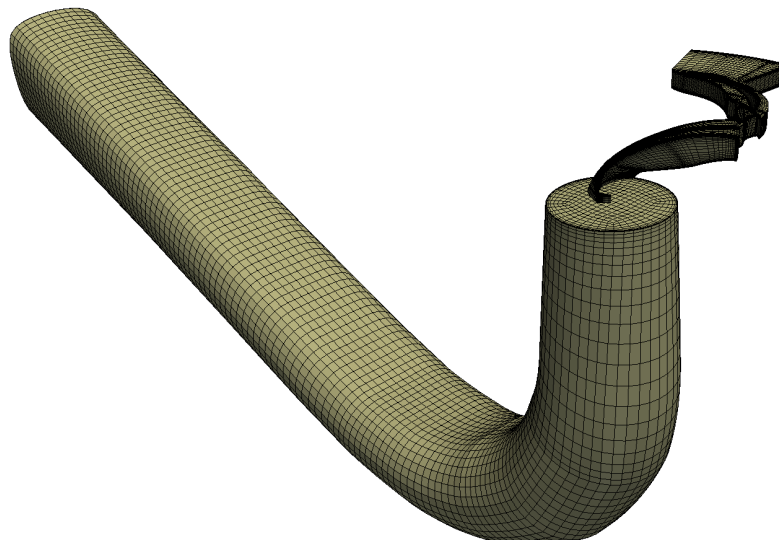


Figure 4.5: Total mesh of the one passage model

the inlet with an incident angle of 9 degrees. This angle places the stagnation point in the center of the stay vane. A uniform turbulent intensity of 0.05 and a turbulent length scale of 0.01m are set at the inlet condition, considering medium turbulence in the incoming flow. All walls are enhanced with no slip boundaries and are assumed to be perfectly smooth. The general grid interface (GGI), connects the opposing periodic faces of the distributor and the runner. The stationary parts of the Francis turbine are also connected via the general grid interfaces. The frozen rotor interface connects the rotating and stationary domain by conserving the interface flux. The outlet is modeled with the opening condition allowing a reentering flow, with a Dirichlet boundary condition for the pressure (0Pa). The fully coupled solver's convergence is assessed by a number of criteria (monitor points and global variables) and the solver aborts the run automatically, after satisfying the specified minimum residues. The defined monitoring points and the global variables are set according to the available experimental data. The solver setup is briefly summarized in table 4.2.

Table 4.2: Computation model summary of the steady-state *commercial code* one passage model

Computational Domain	One passage
Operating point	BEP
Cells	Hexahedron
Grid type	Block structured grid, structured refinement
y_{mean}^+	30
Code	<i>Commercial code</i>
Analysis type	Incompressible steady-state
Advection term	High resolution
Turbulence	High resolution
Convergence criteria	residue of 10^{-8}
Turbulence model	$k\omega$ -SST
Inlet	subsonic mass flow inlet
Outlet	opening condition, Dirichlet BC for the pressure
Walls	smooth, no slip
Interfaces	Stator/rotor (GGI) Frozen rotor, conservation of flux; Stator/stator (GGI)
Fluid	continuous incompressible isothermal Newtonian water

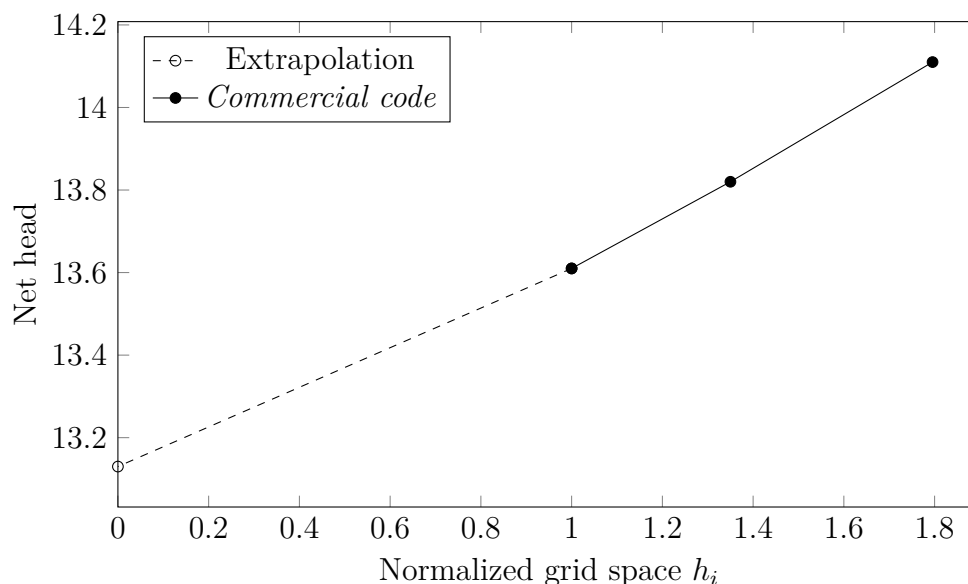
4.2 Grid independence study - steady-state simulation

In the BEP, a grid independence study shows monotonic convergence for global quantities using three different refinement states based on $y_{mean}^+ \sim 30$. Index 1 corresponds to the fine grid, index 2 refers to the medium (reference) mesh density and index 3 to the coarse mesh. As suggested in the corresponding guideline, a uniform grid refinement ratio of greater than 1.3 is used. The performed grid convergence procedure follows the ASME guideline of reporting uncertainties in fluid dynamics [25]. To avoid computational costs the grid study is performed with the one passage model.

The three different grid refinements of the $y_{mean}^+ \sim 30$ grid are reported in table 4.4. In order to limit computational costs, a total cell number of 5M for the full model is the overall goal. The uncertainty of this grid is quantified by the GCI, based on Richardson extrapolation with three grids. Having three uniformly refined grids, the order of convergence p_G is calculated and judged by the formal order of the numerical scheme. One coarser and one finer discretized solution, estimate the medium grids numerical uncertainty, as suggested by Roache to quantify the error of the computational grid. The grid convergence study is summarized in table 4.3.

Table 4.3: Summary of the grid convergence method of the $y_{mean}^+ \sim 30$ grid; numerical uncertainty of the net head and the efficiency

Quantity G	Unit	H	η
Measurement	-	11.91	92.61
r_{21}	-	1.35	1.35
r_{32}	-	1.33	1.33
G_1	-	13.61	87.88
G_2	-	13.82	87.57
G_3	-	14.11	86.79
G_{ext}	-	13.13	88.08
pG	-	1.22	3.21
GCI_{32}	%	6.02	0.69
GCI_{21}	%	4.43	0.28

**Figure 4.6:** Monotonic convergence of the net head

The net head and the efficiency of the Tokke turbine show monotonic convergence, as illustrated in figure 4.6 and 4.7, respectively. The net heads order of convergence is 1.22. The tendency of the estimated net head directs towards the experimental value. The GCI of the extrapolated net head

$$H_{ext} \approx H_1 + \frac{H_1 - H_2}{r^{p_H} - 1} \quad (46)$$

is in the tolerated range for the $y_{mean}^+ \sim 30$ grid with a value of 6%.

The order of convergence for the efficiency is higher than the order of the numerical scheme. Since the efficiency is a combination of two global quantities, the order of

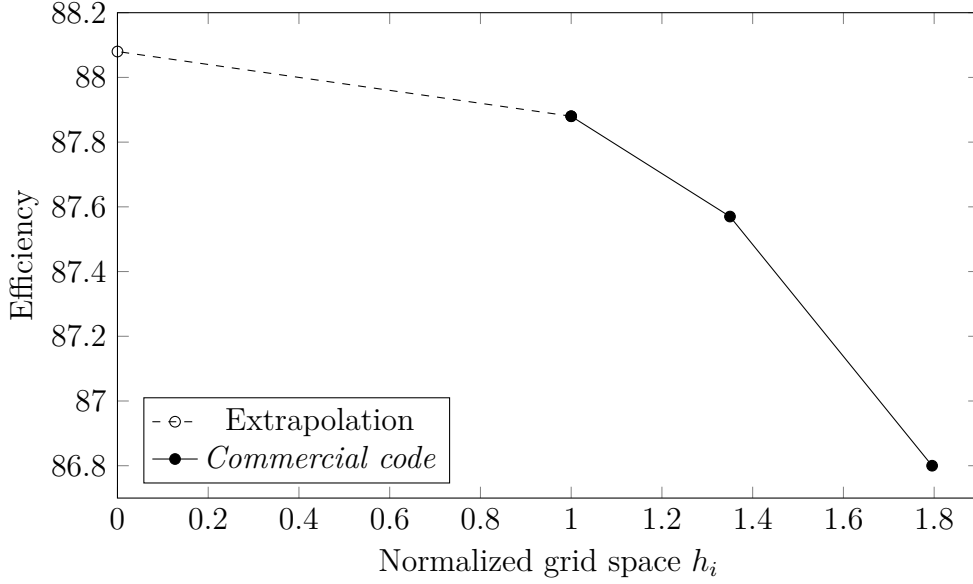


Figure 4.7: Monotonic convergence of the net efficiency

convergence depends on two individual global quantities.

$$\eta_{\text{ext}} \approx \eta_1 + \frac{\eta_1 - \eta_2}{r^{p_\eta} - 1} \approx C \frac{T_1 + \frac{T_1 - T_2}{r^{p_T} - 1}}{H_1 + \frac{H_1 - H_2}{r^{p_H} - 1}} \approx C \frac{T_1}{H_1} + C \frac{T_1 - T_2}{H_1 - H_2} \left[\frac{1}{C} \frac{1}{r^{p_T} - 1} \left(1 + \frac{H_1 - H_2}{H_1(r^{p_H} - 1)} \right) \right] \quad (47)$$

From this equation the formal order of convergence for the efficiency is estimated by

$$p_\eta \approx \frac{\log \left[\left[\frac{1}{C} \frac{1}{r^{p_T} - 1} \left(1 + \frac{H_1 - H_2}{H_1(r^{p_H} - 1)} \right) \right]^{-1} + 1 \right]}{\log(r)} = 3.3 \quad (48)$$

. This value is very close to the computed efficiency convergence order. Since the order is high, the GCI value is in the superior range with 0.7% for the reference grid. An additional possibility of a high convergence order might originate from the cancellation of errors [24].

The grid convergence method verifies the ability of monotonic convergence of the medium (reference) grid. All further computations are based on this grid type meeting computational efficiency and validity of the calculated quantities. In contrast to the domain extension of the grid study, the following numerical studies are conducted by considering the full model domain and the medium mesh refinement of the grid study.

4.3 Numerical setup - Steady-state simulation

Grid

The full model's distributor mesh is separated at two additional interfaces. One interface is located between the outer spiral case (SC) and the stay vane section (SV). The second interface connects the stay vanes and the adjustable guide vanes (GV) of the distributor. Figure 4.8 shows the obtained final grid of the SC and SV section. The blocking of the components was provided by [4].

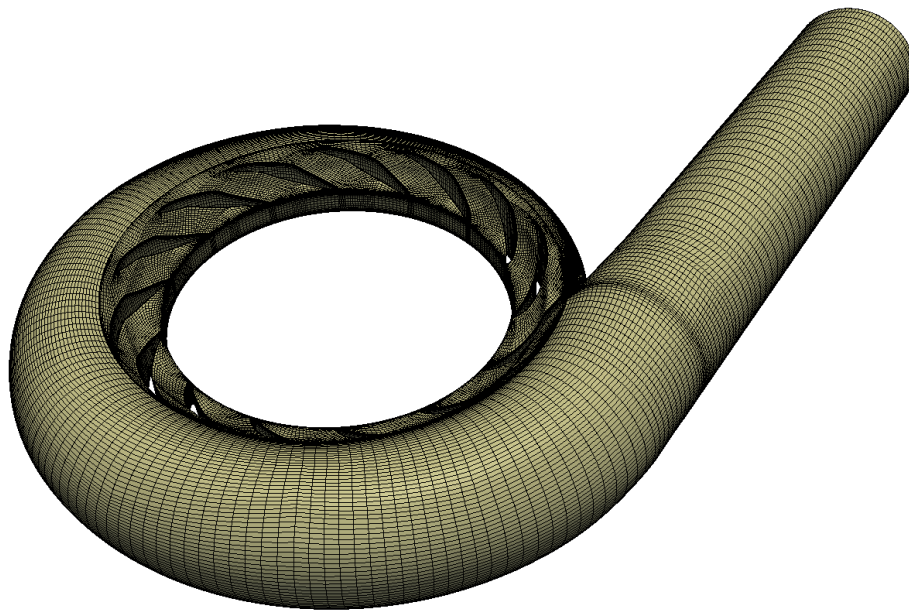
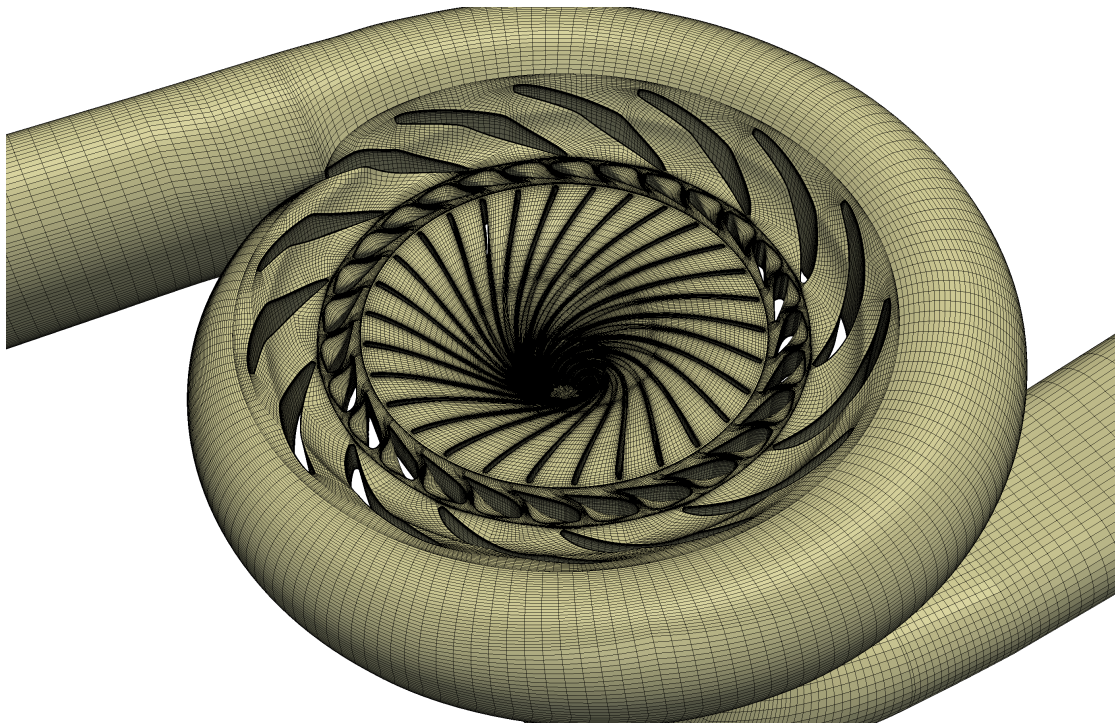


Figure 4.8: Mesh structure $y_{mean}^+ \sim 30$ of the full model's spiral case

The guide vane's mesh differs slightly for all three operating points (PL, BEP and HL), since the guide vane angle changes. The one passage model's medium meshes of the guide vane and the runner (RN) are mapped to a fully rotational domain (figure 4.9) to fit the full model setup. The draft tube's (DT) medium mesh of the one passage model, propagates the flow towards the outlet boundary.

Table 4.4: Mesh grid summary of the full model's grid

Grid	Full model
Spiral case	511k
Stay vanes	610k
Guide vanes	1695k
Runner	2177k
Draft tube	268k
Total cells	5260k
Determinant	>0.22
Angle	>12°
Refinement ratio	1.3

**Figure 4.9:** Mesh details of the full model's grid

Solver setup

The full model's mesh is used to set up a steady-state flow simulation in *commercial code*. The flow domain is separated into the relevant sub-domains (spiral case, stay vane, guide vane, runner and draft tube). During the steady-state simulation all three operating conditions are considered to show the capabilities of the simulation tool in the characteristic conditions. The fluid properties are chosen according to the operation points (PL, BEP and HL) in table 3.1. The RANS equations are closed by the two equation turbulence model $k\omega$ -SST, using automatic wall functions. A simple subsonic mass flow is applied at the inlet perpendicular to

the inlet surface of the spiral case. A uniform turbulent intensity of 0.05 and a turbulent length scale of 0.01m, are set at the inlet condition, considering medium turbulence in the incoming flow. All walls are enhanced with no slip boundaries and are assumed to be perfectly smooth. The stationary parts of the Francis turbine are connected at the interface through general grid interfaces. Mixing plane interfaces, connect the rotating and stationary domain by the stage average velocity downstream constraint at the interfaces. The turbine axis of rotation is the negative z-axis of the coordinate frame. The outlet is modeled with the opening condition allowing a reentering flow, with a Dirichlet boundary condition for the pressure (0Pa). The fully coupled solver's convergence is assessed by a number of criteria (minimum residues, monitoring points and global variables). The defined monitoring points and the global variables are set according to the available experimental data. The solver setup is briefly summarized in table 4.5.

Table 4.5: Computation model summary of the steady-state *commercial code* full model

Computational Domain	Full model
Operating points	PL, BEP and HL
Cells	Hexahedron
Grid type	Block structured grid, structured refinement
y_{mean}^+	30
Code	<i>Commercial code</i>
Analysis type	Incompressible steady-state
Advection term	High resolution
Turbulence	High resolution
Convergence criteria	residue of 10^{-8}
Turbulence model	$k\omega$ -SST
Inlet	Subsonic mass flow inlet
Outlet	Opening condition, Dirichlet BC for the pressure
Walls	Hydraulically smooth, no slip
Interfaces	Stator/rotor (GGI) Stage mixing model, stage average velocity; Stator/stator (GGI)
Fluid	Continuous incompressible isothermal Newtonian water

4.4 Numerical setup - Unsteady simulation

4.4.1 Solver setup - *Commercial code*

The grid is the same as the one used in the steady-state simulation, with 5M cells. During the unsteady simulation all three operating conditions are considered to show the capabilities of the simulation tool in the characteristic conditions. The fluid properties are chosen according to the operation points (PL, BEP and HL) in table 3.1. Initialization of the fluid domain is based on the steady-state simulation results. A total time corresponding to one rotation is chosen with a resolution of 1.006 degree in the BEP condition. The time is discretized by a second order backward Euler scheme. The remaining parameters of the unsteady simulation are chosen according to the steady-state simulation.

The stationary parts of the Francis turbine are connected at the interface via a general grid interfaces.

Table 4.6: Computation model summary of the unsteady *commercial code* full model

Computational Domain	Full model
Operating points	PL,BEP and HL
Cells	Hexahedron
Grid type	Block structured grid, structured refinement
y_{mean}^+	30
Code	<i>Commercial code</i>
Analysis type	Incompressible unsteady, total computation time corresponding to one rotation of the turbine, with a resolution of 1.006 degree in the BEP condition
Transient num.	Second order backward Euler
Advection term	High resolution
Turbulence num.	High resolution
Convergence criteria	max residue of $< 10^{-8}$
Turbulence model	$k\omega$ -SST
Inlet	Subsonic mass flow inlet
Outlet	Opening condition, Dirichlet BC for the pressure
Walls	Hydraulically smooth, no slip
Interfaces	Stator/rotor (GGI) Unsteady rotor-stator interface, conservation of interface flux; Stator/stator (GGI)
Fluid	Continuous incompressible isothermal Newtonian water

Unsteady rotor-stator interfaces connect the rotating and stationary domains by conserving the interface flux. The solver setup is briefly summarized in table 4.6.

4.4.2 Solver setup - *OpenFoam*

To investigate the capabilities of the free software package *OpenFoam*, an unsteady flow simulation is set up. The grid is the same as the one used in the *commercial code* simulations, to maintain comparability. In *OpenFoam* only the BEP condition is investigated. The Newtonian fluid properties are chosen according to the operation condition in table 3.1.

Table 4.7: Computation model summary of the unsteady *OpenFOAM* full model

Computational Domain	Full model
Operating point	BEP
Cells	Hexahedron
Grid type	Block structured grid, structured refinement
y_{mean}^+	30
Code	<i>OpenFoam 2.3.1</i>
Analysis type	Incompressible unsteady, total computation time corresponding to five rotations of the turbine, with a resolution of $CFL < 5$
Transient num.	Second order backward
Advection term	Second order
Turbulence num.	Second order
Convergence criteria	$res_p < 10^{-7}$ and $res_{U,k,\omega} < 10^{-5}$
Turbulence model	$k\omega$ -SST
Inlet	U,k, ω Dirichlet; p Neumann
Outlet	U,k, ω Neumann; p Dirichlet
Walls	Hydraulically smooth, no slip
Interfaces	cyclicAMI
Fluid	Continuous incompressible isothermal Newtonian water

Initialization of the fluid domain is based on uniform fields for the variables p, U, k and ω . A total time corresponding to five rotations¹ is taken with a variable time resolution corresponding to a CFL-number (Courant-Friedrichs-Lewy-number) less than five. The turbulence is modeled by a RANS two equation $k\omega$ -SST turbulence model, using automated wall functions. A uniform Dirichlet inlet condition for the velocity ($U_{in} = Q/A_{in} = 2.323\text{m/s}$) is set perpendicular to the inlet surface of the spiral case. A uniform turbulent intensity of $I = 0.05$

$$k_{in} = \frac{3}{2}(U_{in}I)^2 = 0.0203 \frac{\text{m}^2}{\text{s}^2} \quad (49)$$

¹The lengthy computation was not carried out until the preferable final time, since the computational process showed typical convergence.

and a turbulent length scale of $l_t = 0.01\text{m}$

$$\omega_{in} = C_\mu^{-1/4} \frac{\sqrt{k}}{l_t} = 26.03 \frac{1}{\text{s}} \quad (50)$$

is set at the inlet condition, considering a medium turbulence in the incoming flow.[26]

All walls are enhanced with no slip boundaries and are assumed to be hydraulically smooth. The separated parts of the Francis turbine are connected at the interface via an arbitrary mesh interface (AMI). The outlet is modeled with a Neumann boundary for the velocity, and a Dirichlet boundary condition for the pressure (0Pa, reference). Combining the SIMPLE (relaxation factors to increase stability) and PISO algorithm (PIMPLE), convergence is assessed by the residuals ($res_p < 10^{-7}$ and $res_{U,k,\omega} < 10^{-5}$). Second order schemes are chosen to evaluate the numerical approximations. The defined monitoring points and the global variables are set according to the available experimental data. The solver setup is briefly summarized in table 4.7.

5 Results

In this section the results of the previously discussed model setups are presented and compared to the experimental data. At first, the deviations of the global quantities and the mean values of the static pressure are validated against the provided data. Thereafter, the velocity data is investigated and compared to available literature of the Tokke model turbine. The unsteady properties of the fluctuating pressure in the turbine are discussed in the time domain and the frequency domain. Finally, the losses in the distributor and the draft tube are pointed out.

5.1 Integral quantities

The measured data of the integral quantities are summarized in table 3.1 for all three operating points. The relative deviations $G\%$ of the computed integral quantities G_{CFD} to the experimental data G_{EXP}

$$G\% = \frac{G_{CFD} - G_{EXP}}{G_{EXP}} \quad (51)$$

are reported in table 5.1. The integral values H and T are computed by the mass flow average of the local quantities on the corresponding surfaces. All unsteady simulation results are averaged over the last 180 time steps, corresponding to one half rotation. The steady-state simulation quantities are averaged over the last 100 iterations. The hydraulic efficiency, estimated with the CFD software η_{CFD} , is given by the equation

$$\eta_{CFD} = \frac{(T - T_{fr})\omega_r}{\rho g H Q} \quad (52)$$

incorporating the friction torque of the seals. The deviation to the experimental value reported in table 5.1 is defined as

$$\eta\% = \eta_{CFD} - \eta_{EXP} \quad (53)$$

Commercial code: Both the unsteady and steady-state simulation, obviously show correlations in the results at the BEP and HL regime. Generally, the torque and

the net head are overestimated by *commercial code* at these operating points. The deviations of the estimated values lie in a range $G_{\%} < 10\%$. The two global quantities are not captured well, but since they deviate in a similar way, the estimated hydraulic efficiency is predicted surprisingly well, with $\eta_{\%} < 1.5\%$.

In PL no obvious trend of the integral quantities is evident. Generally, the deviations are higher compared to the other operating points. Due to stability problems in *commercial code* the numerical scheme modeling turbulence was reduced to first order. The steady-state simulation in *commercial code* underestimates the absolute value of the integral quantities, whereas the unsteady simulation overestimates those quantities.

The general tendency of over-estimating the global quantities H , T goes back to the fact that several losses are ignored. The friction torque and leakage flow through the seals are not considered in the CFD simulation, but result in additional losses. Thus, losses due to the friction are compensated by the experimental friction torque. Jošt *et al.* [6] estimated the friction and the volumetric losses using the $k\omega$ -SST-CC-KL turbulence model in their CFD simulation, which can be used for further compensation. Generally, the finer grid's solution has a smaller deviation from the experimental values compared to the simulation results of Lenarcic *et al.* [4]. The unsteady results behave qualitatively similarly as in the simulation presented by Trivedi *et al.* [8].

OpenFoam deviates more than the *commercial code* simulation results for the head and the hydraulic efficiency, and deviates less for the torque.²

Table 5.1: Relative deviations of integral quantities between computed results and measurements using *OpenFoam*(OF)/*Commercial code*(COM), steady-state(S)/unsteady(US) simulation

OP	Config	Unit	H	T	η
PL	COM, S	%	-4.38	-10.38	-8.99
	COM, US	%	6.38	18.47	4.87
BEP	OF, US	%	20.11	2.23	-13.22
	COM, S	%	8.36	8.86	-0.33
	COM, US	%	9.29	9.99	-0.16
HL	COM, S	%	2.28	3.96	1.11
	COM, US	%	3.07	5.09	1.4

²The computation was not carried out until the preferable final time, since the computational process showed typical convergence.

Summary global quantities Both the unsteady and steady-state simulations, show obvious parallels in their results at the BEP and HL regime. Generally the torque and the net head are overestimated by *commercial code* at these two operating points. The deviations of the estimated values lie in a range $G\% < 10\%$. The two global quantities are not captured well, but since they deviate similarly, the estimated hydraulic efficiency is predicted surprisingly well $\eta\% < 1.5\%$. In PL no obvious trend of the integral quantities is evident, but the deviations are higher compared to the other operating points $\eta\% < 9\%$. The simulation using a finer grid allowed more accurate results compared to the simulation results of Lenarcic *et al.* [4]. The unsteady results behave qualitatively similar to the simulation presented by Trivedi *et al.* [8]. Including the runner side spaces may result in a further improvement of the predicted global quantities. *OpenFoam* is not capable of predicting the efficiency compared to the experimental data and *commercial code*. The efficiency deviates by $\eta\% = -13.2\%$.

5.2 Mean static pressure

The measured time series data of the static pressure probes, is available on the Francis 99 workshop webpage [1]. The time averaged pressure values at the evaluated locations are summarized in table 5.2.

Table 5.2: Pressure data at the pressure sensor locations (VL01, DT11, DT21, P42, P71, S51)

OP	Unit	VL01	S51	P42	P71	DT11	DT21
PL	kPa	175.45	94.66	104.91	88.77	101.55	101.38
BEP	kPa	171.64	103.70	117.65	100.11	102.78	102.28
HL	kPa	182.64	103.82	118.10	99.43	101.65	100.78

The relative deviations $p\%$ of the computed pressure probes p_{CFD} compared to the experimental values p_{EXP}

$$p\% = \frac{p_{CFD} - p_{EXP}}{p_{EXP}} \quad (54)$$

are reported in table 5.3. The pressure level is adjusted according to the mismatch between the experimental data and the Dirichlet boundary condition of the static pressure in the numerical simulation. The static pressure data is averaged over the last 180 physical time steps in the unsteady simulation, or over the last 100 iterations of the steady-state simulation.

Table 5.3: Relative deviations of static pressure between computed results and measurements using *OpenFoam*(OF)/*Commercial code*(COM), steady-state(S)/unsteady(US) simulation

OP	Config	Unit	VL01	S51	P42	P71	DT11	DT21
PL	COM, S	%	0.36	3.65	7.83	4.43	-2	-1.86
	COM, US	%	2.36	5.45	7.29	5.12	-2.03	-2.14
BEP	OF, US	%	8.4	-1.6	6.2	-2.9	-6.6	-6.5
	COM, S	%	4.36	8.56	4.17	4.67	-2.64	-2.15
	COM, US	%	5.26	8.47	4.18	4.64	-2.64	-2.14
HL	COM, S	%	-2.44	4.86	2.53	0.16	-7.34	-6.52
	COM, US	%	-1.85	5.08	2.91	0.2	-7.34	-6.51

In *commercial code* a maximum relative deviation of the static pressure occurs at the measuring point S51 on the suction side of the runner blade, with a value of $p\% < 8.6\%$. Generally, the static pressure data is conform to the experimental data. The CFD simulation overestimates the average static pressure in the rotating domain, and underestimates the average static pressure in the draft tube. In summary, some flow phenomena are not captured by the flow simulation in the region of the runner draft tube interface. The information of the fluctuating pressure is discussed in section 5.4.

These results are in accordance with the simulation of Nicolle and Cupillard [2] and Buron *et al.* [3]. Compared to the simulation results of Lenarcic *et al.* [4], the relative pressure deviation of the steady-state and unsteady flow simulation show no improvement and the same tendency.

Compared to the results of *commercial code*, *OpenFoam* predicts the pressure data in the acceptable range. The highest deviation occurs at the sensor location VL01 with a static pressure deviation of $p\% < 9\%$.

Summary mean pressure In the *commercial code* simulation a maximum relative deviation of the static pressure occurs at the location S51 on the suction side of the runner blade with a value of $p\% < 8.6\%$. Since the pressure probes in the runner are overpredicted and in the draft tube underpredicted some flow phenomena are not captured accurately in this region. These results are in accordance with the simulation of Nicolle and Cupillard [2], Buron *et al.* [3] as well as Lenarcic *et al.* [4]. The local static pressure data estimated by *OpenFoam* shows a similar tendency as the results of the *commercial code* simulation.

5.3 Averaged velocity field in the draft tube

The time averaged data of the velocity measurements at the top and bottom line in the draft tube are available on the Francis 99 workshop webpage [1]. The time averaged velocity data in figure 5.1 to figure 5.3 are labeled as LDA. A abscissa value of $r/r_0 = 0$ indicates the center of the draft tube, whereas a value of $r/r_0 = 1$ refers to the smooth wall of the draft tube. The CFD velocity data is averaged to mimic the provided averaged LDA measurement data and illustrate the similarities. The steady-state simulation results are averaged over the 100 most recent values and the unsteady time average values are computed by considering the last 100 time steps. The velocity probes' locations of the experiment and CFD simulation, coincide to maintain comparability of the results. Between the simulation results linear splines fit a continuous curve through the estimation. In PL and HL only steady-state and unsteady simulations in *commercial code* are performed.

At PL, the CFD data captures the experimental velocity profile accurately (figure 5.1), even though the order of the turbulent numerical scheme was lowered to the first order. In the PL condition the characteristic swirl rotating in the runner's direction is captured correctly in the draft tube. The maximum is located in the near wall region. The stream-wise velocity profile indicates that in the middle of the draft tube reverse flow occurs until a normalized diameter of about $r/r_0 < 0.7$. Outside this stagnation zone a strongly discharged region is located between $0.7 < r/r_0 < 1$. This phenomena is typical for the top and the bottom line in the draft tube. Compared to the BEP and HL, the discrepancy in the PL condition is surprisingly low. This fact meets the results of several papers [4], [5]. Towards the wall the $k\omega$ -SST turbulence model with automatic wall functions cannot capture the boundary layer in stream-wise direction. As mentioned by Lenarcic *et al.* [4] this can be attributed by the applied standard wall functions, limiting the resolution of the boundary layer. At the bottom line, the circumferential velocity component is slightly underestimated. Generally, steady-state and time averaged unsteady results correspond, indicating no unsteady effects in the draft tube.

The *commercial code* simulation in the BEP condition (figure 5.2) captures the experimental velocity profile in the stream-wise direction precisely, except for the region near the runner's rotational axis $r/r_0 < 0.2$. However, the experimental velocity decreases only moderately in this region. A strong counter-rotating swirl is predicted incorrectly by the CFD simulation. This swirl may be the reason for the deviation in the stream-wise direction near the rotational axis. The circumferential velocity profile overestimates the experimental data in the region ($0.1 < r/r_0 < 0.7$) of the swirl strongly. The steady-state and time averaged unsteady result are

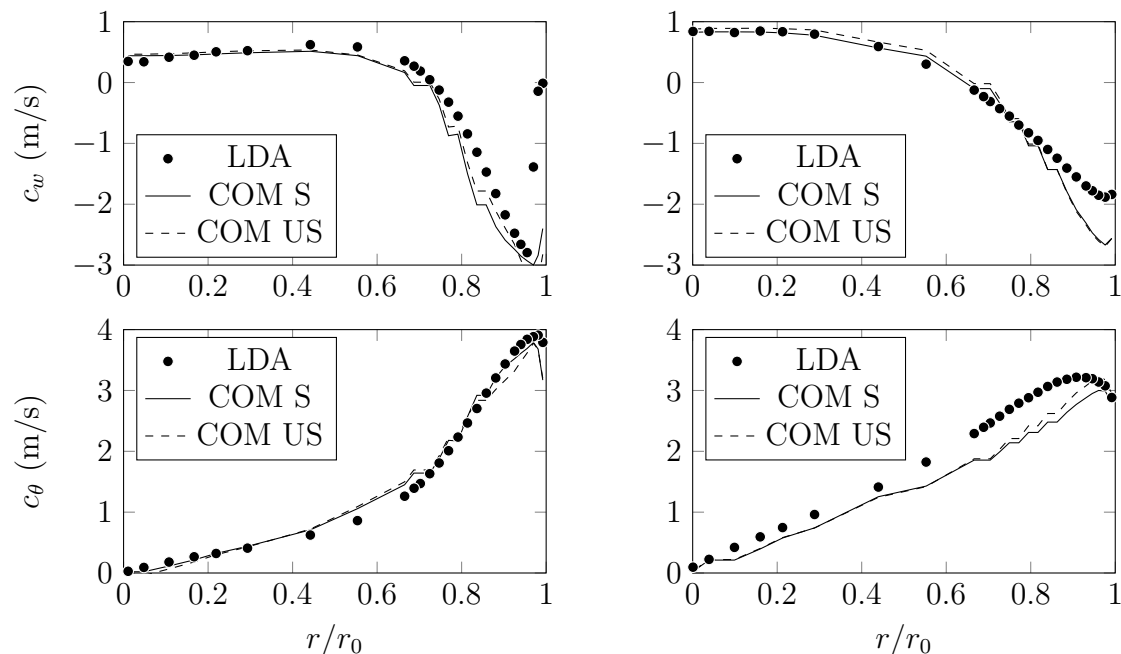


Figure 5.1: Results of the axial velocity (top) and circumferential velocity (bottom) on the top line (left) and bottom line (right) at operating point PL

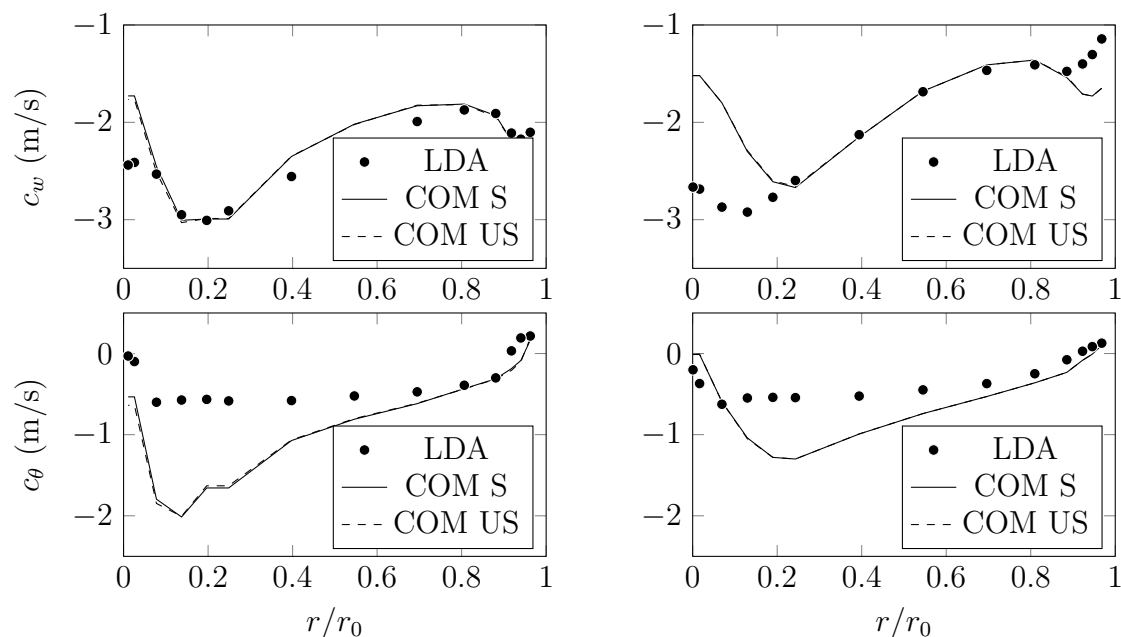


Figure 5.2: Results of the axial velocity (top) and circumferential velocity (bottom) on the top line (left) and bottom line (right) at operating point BEP

in good accordance at the BEP. The additional refinement considered in this work does not affect the simulated averaged velocity profile significantly, compared to Lenarcic *et al.* [4]. Compared to the experimental data, the swirl intensity is predicted incorrectly, since a stronger vortex is formed in the simulation at BEP

condition and not at the HL condition. The discrepancy of the circumferential velocity is addressed by Aakti *et al.* [5].

The simulation of the HL condition (figure 5.3), captures the experimental velocity profile in the stream-wise direction precisely, except for the region near the runner's rotational axis $r/r_0 < 0.2$. Due to the small deviation in the prescribed operating point, the results of the HL condition and the BEP condition are very near to one another. A counter-rotating swirl is predicted by the CFD simulation, which correspond to the measurement data at the HL regime.

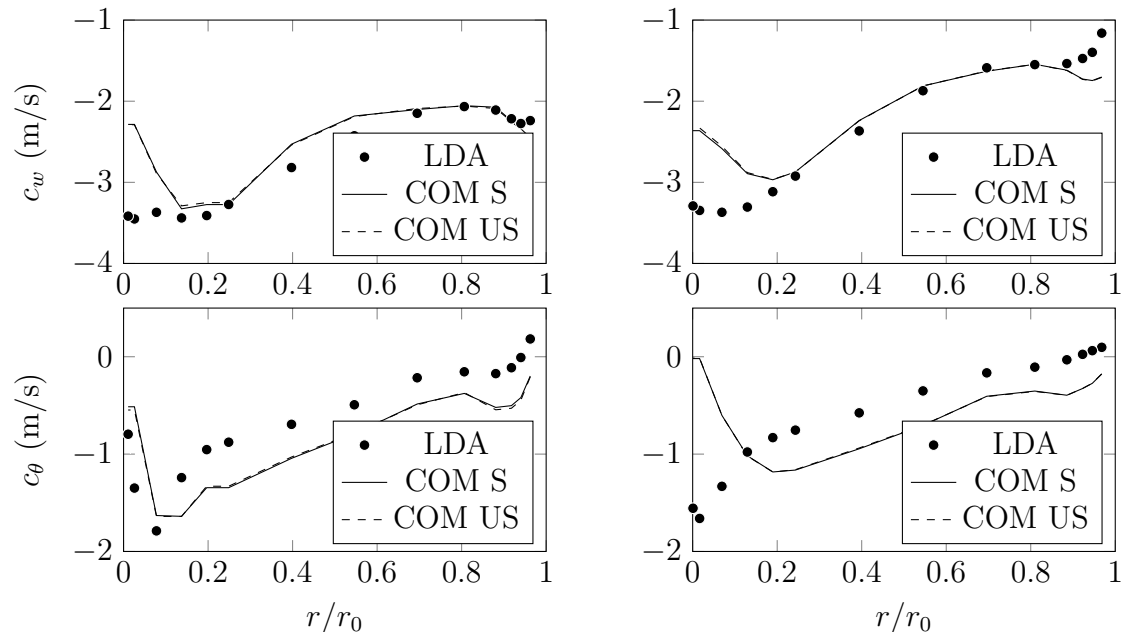


Figure 5.3: Results of the axial velocity (top) and circumferential velocity (bottom) on the top line (left) and bottom line (right) at operating point HL

The over-prediction of swirl in the region $0.1 < r/r_0 < 1$ can be the reason of the deviation in the stream-wise direction at the rotational axis. In difference to the BEP, the concentrated swirl is predicted slightly better. The prediction of the top and the bottom line are similar. Steady-state and time averaged unsteady result agree highly at the HL operating point. As for the BEP, the averaged velocity components are similar to the results of Lenarcic *et al.* [4].

Summary mean velocities Steady-state and time averaged unsteady results are in excellent correlation, indicating no unsteady effects in the draft tube velocity profile. The velocity profiles in the PL condition are estimated surprisingly well. At the BEP and the HL conditions, a strong swirl is predicted, which has no similarities to the experimental data. The computed velocity profile coincides with the profiles computed by Lenarcic *et al.* [4] and Aakti *et al.* [5].

5.4 Pressure fluctuation

Furthermore, time dependent pressure data at the described probe locations was provided by the Francis 99 workshop in the three given operating conditions (PL, BEP and HL). The unsteady CFD simulation was also set up for PL, BEP as well as HL and the time dependent pressure data was estimated at the same locations. The simulated and the experimental data at all three operating points are depicted in figure 5.4 to 5.6.

Generally, the characteristic sinusoidal frequency of the pressure fluctuations p' is captured with respect to time domain. The probes at the wall of the draft tube are insufficiently reproduced in all three operating conditions. In the other points, the dominant frequency and the amplitudes are captured, but pressure peaks are highly damped out. Thus, the pressure spikes at the suction and pressure side of the full length blade, are not estimated at all by the CFD simulation.

Using FFT the temporal data set is transformed to the frequency-amplitude domain. The pressure amplitudes \hat{p} are plotted as a function of the normalized frequency f_{FT}/n , where f_{FT} corresponding to the frequency and n to the runner's rotational frequency. The pressure fluctuations in the frequency domain are illustrated in figure 5.7 to 5.10.

The mean components of the static pressure data (presented in section 5.2) are subtracted from the unsteady pressure data to reveal only the fluctuating pattern.

$$p' = p - \bar{p} \quad (55)$$

The pressure probes name's (DT11, DT21, VL01, S51, P42 and P71), indicate the location of the measuring points. In the figure's legends these denotations refer to the experimental data.

5.4.1 Pressure time domain

The characteristic unsteady pressure fluctuations in PL condition, are summarized in figure 5.4 for the six pressure probe locations. At the two measuring points in the draft tube DT11 and DT21, a long wave pattern can be recognized, referring to the swirl in the draft tube. Higher frequency components are not accurately captured by the simulation. In the vaneless space VL01, the general behavior of the pulsations are reproduced. At the three runner blade sensors, the sinusoidal pattern is estimated, but the less frequent pressure peaks are insufficiently resolved.

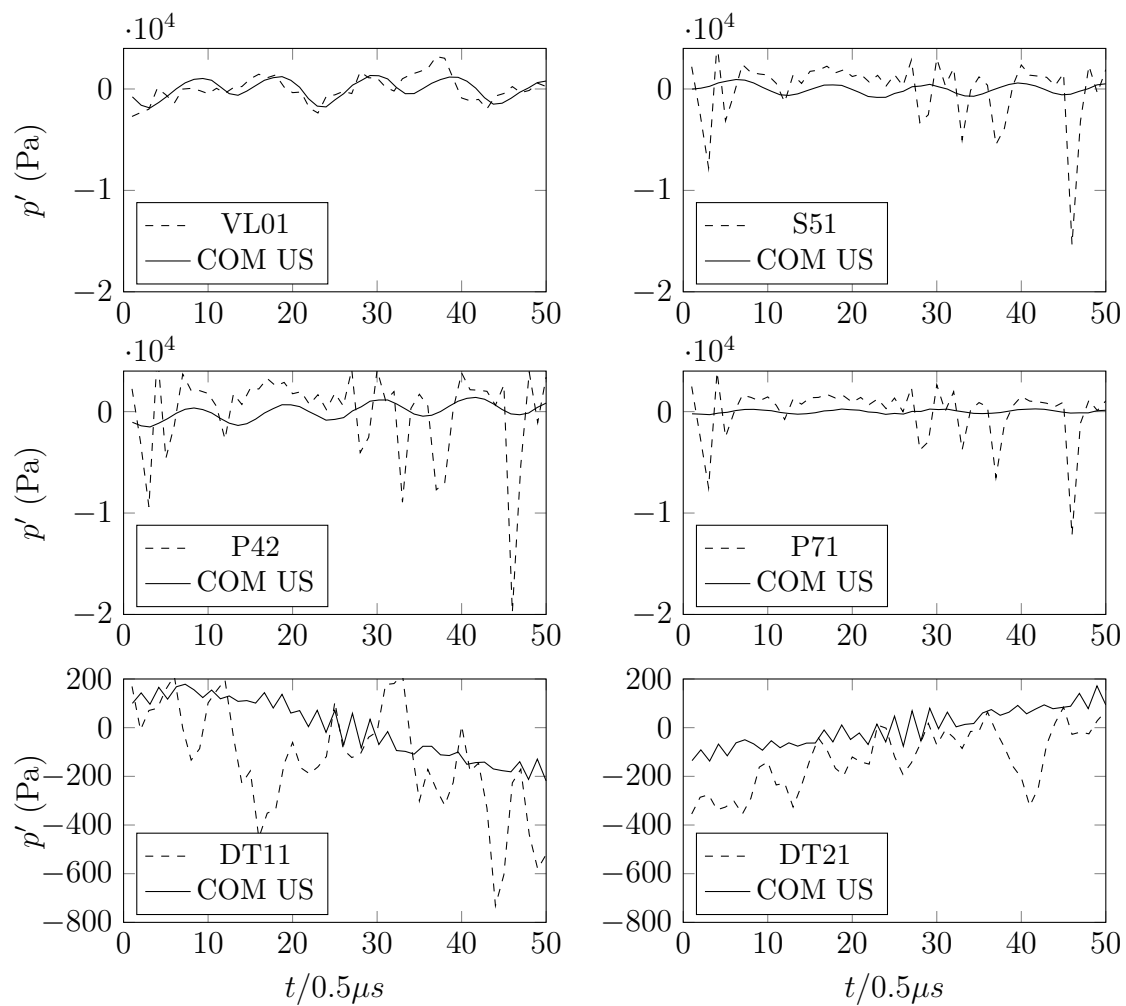


Figure 5.4: Pressure data at operating point PL in real time

The temporal data of the pressure fluctuations in the design point BEP is presented in figure 5.5. The pressure probes at the draft tube's wall and the higher frequent pressure pulsations are insufficiently reproduced by the CFD simulation. At the other locations (VL01, S51, P42 and P71), the dominant frequency and its amplitudes are well captured. The lower frequent pressure spikes at the suction and pressure side of the full length blade are fully dampened.

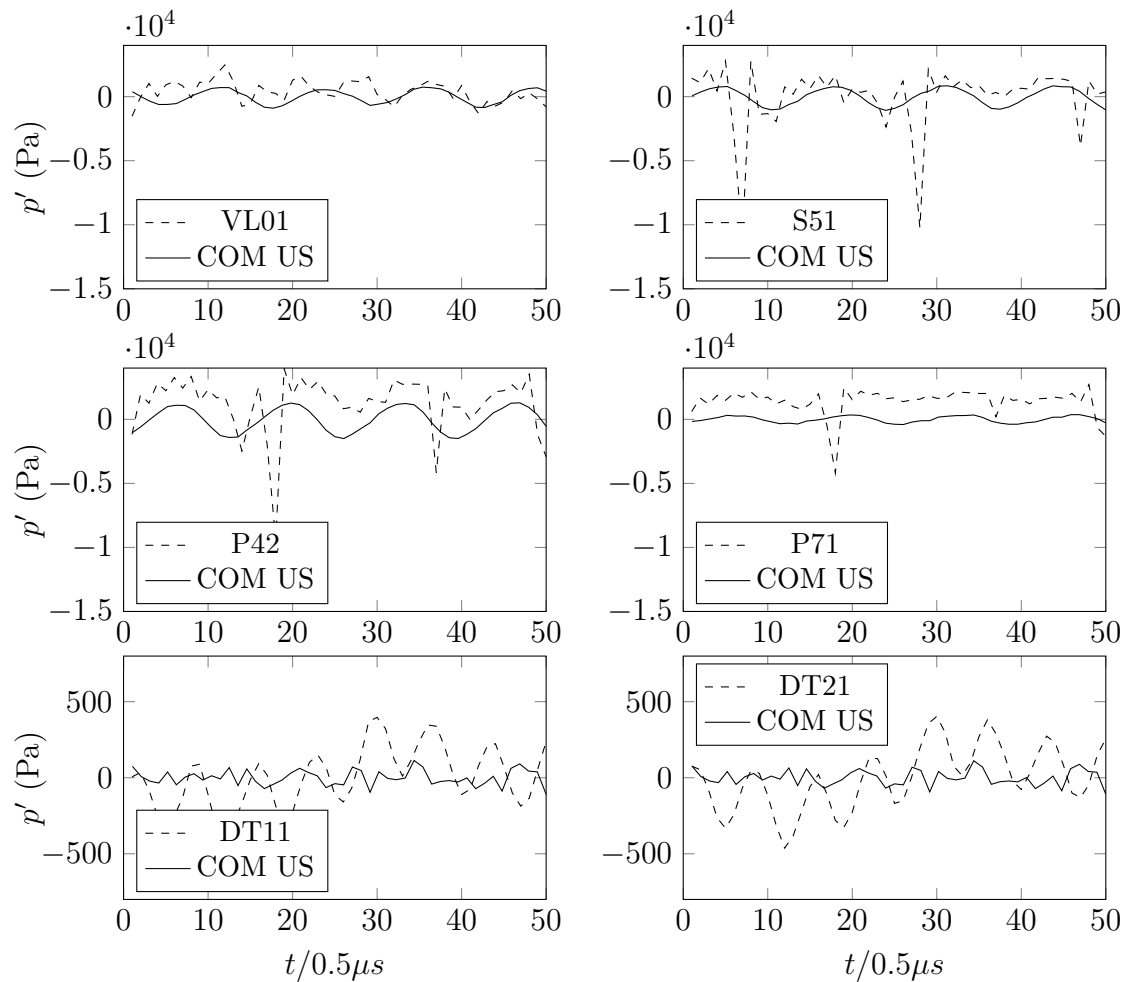


Figure 5.5: Pressure data at operating point BEP in real time

The unsteady pressure fluctuations in HL condition are summarized in figure 5.6. At the draft tube's wall DT11 and DT21, the computed pattern of the CFD simulation has no similarities to the experimental data. In the vaneless space VL01, the general behavior of the pulsations are reproduced accurately. At the three runner blade locations, the general pattern is captured by the simulation. Only the lower frequent pressure spikes are insufficiently resolved in the runner domain. As expected, the two off-design conditions (PL and HL) produce higher pressure amplitudes.

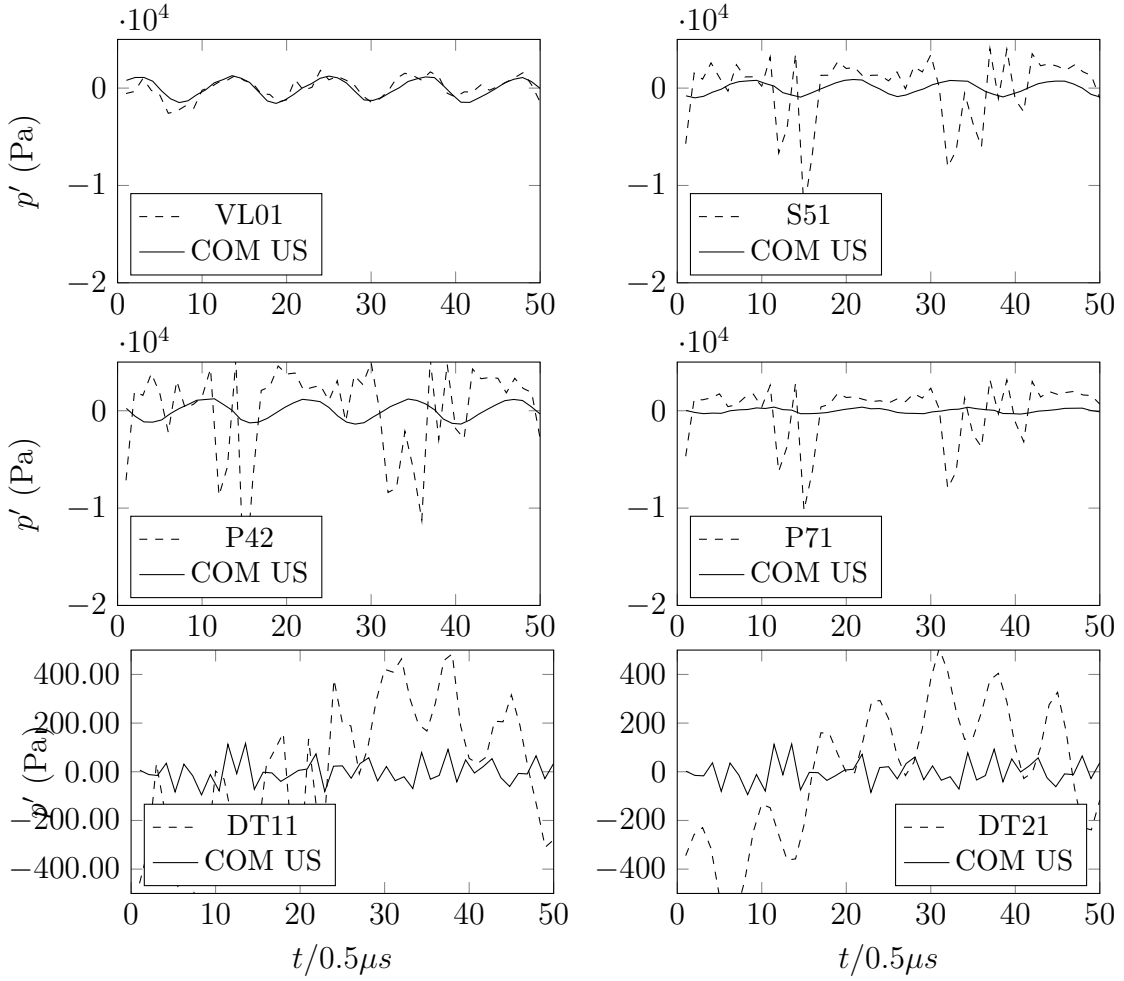


Figure 5.6: Pressure data at operating point HL in real time

5.4.2 Pressure frequency domain

The fluctuating pressure data of the experiments and the CFD simulation is examined in the frequency domain, investigating the linear superposition of characteristic sinusoidal functions. The expected characteristic normalized frequencies f_{FT}/n are described in table 5.4.

The Fourier coefficients are processed using the FFT (fast Fourier transformation) and extracting data up to the Nyquist frequency, which depends on the sample frequency in the time domain. The resolution of the frequencies increases with the total sample size N_p .

$$\hat{p} = \frac{2}{N_p} |\mathcal{F}(p')| \quad (56)$$

The computed pressure amplitudes \hat{p} correspond to the illustrated time domain data. The strongest vibrations are in the PL operating condition at the pressure-

Table 5.4: Dominant normalized frequencies f_{FT}/n occurring in the rotor-stator interaction (RSI)

f_{FT}/n	Description
1	The swirl in the draft tube induces a low frequent pressure fluctuation at the draft tube probes DT11 and DT12.
15	Full length blades, splitter blades cause fluctuations at the locations VL01, S51, P42 and P71.
30	Sum of the full length blades and splitter blades indicate high amplitudes at the locations VL01, S51, P42 and P71. (blade passing frequency)
14	The stay vanes have no clear visible influence on the pressure fluctuation.
28	The 28 guide vane pressure peaks are visible on the pressure and suction side of the full length blades (S51, P42 and P71).
multiples	Multiples of these frequencies occur to all that dominant normalized frequency components listed above.

side of the blade at the location P42.

The Fourier transformed data of the PL condition is presented in figure 5.7. Some of the main frequency components are captured quite well with strong discrepancies at other main features. The deviations are already pointed out in the time domain data at the locations S51, P42 and P71. High pressure peaks occur with a normalized frequency of 15 and 30, which are insufficiently reproduced. The smooth harmonic with a normalized frequency of 28, corresponding to the guide vanes number, is captured in these three locations. In the draft tube the low frequent fluctuation's tendency is predicted referring to the rotation of the swirl. The back-propagation of the passing runner blades is estimated well at the location VL01.

The pressure fluctuations in the BEP condition are presented in figure 5.8. The main components of table 5.4 are captured in the vaneless space VL01. As already pointed out while discussing the time domain data, some frequency components at the locations S51, P42 and P71 are not present at all. As indicated for the other operating points, the high pressure peaks at a normalized frequency of 15 and 30 are not predicted. The smooth harmonic with a normalized frequency of 28 corresponding to the guide vanes number is captured in these three locations. In the draft tube, no significant pattern is estimated by the simulation. The simulation results agree with the results obtained by Stoessel and Nilsson [27] using

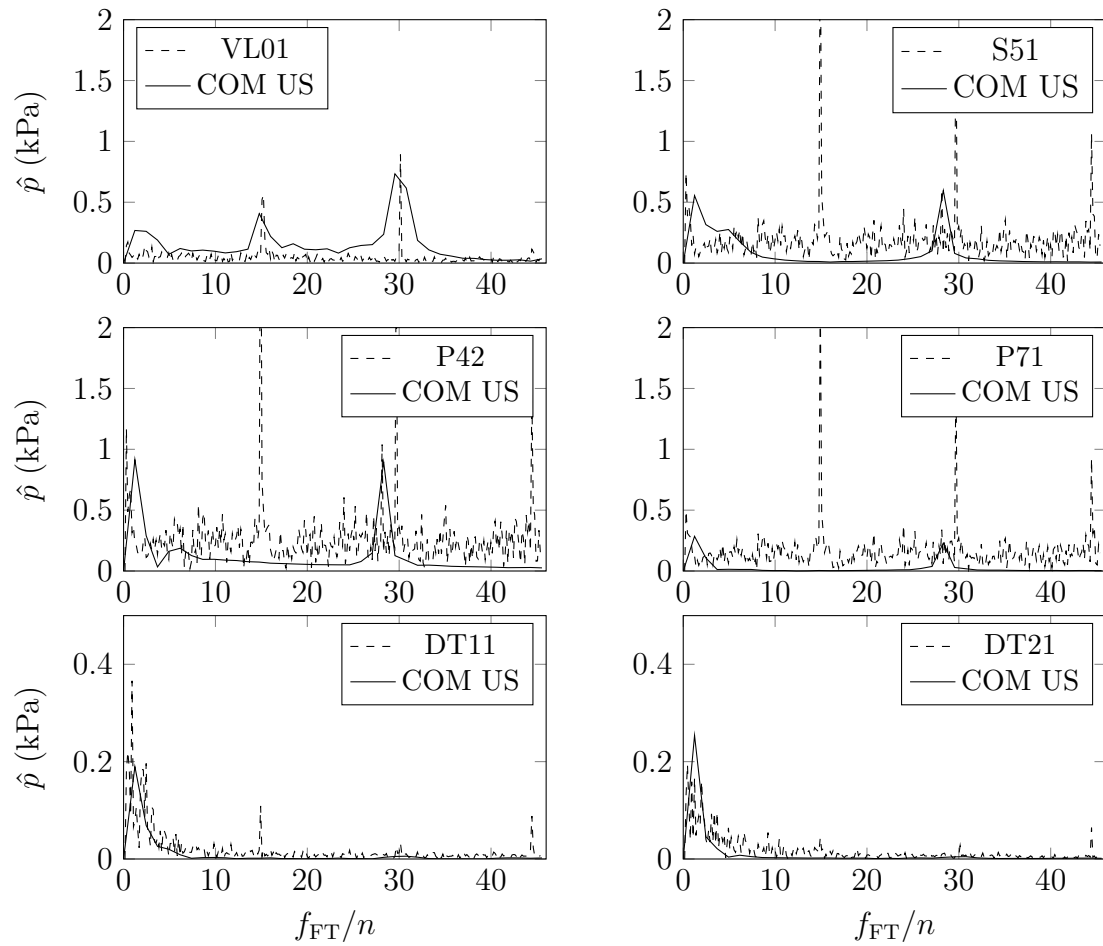


Figure 5.7: FFT of the pressure data at the PL operating condition

the $k\epsilon$ turbulence model and Buron *et al.* [3] using Spalart-Almaras turbulence model.

Figure 5.9 shows the pressure field in the BEP in the vaneless space. At the contours of the plot the blade passing frequency of the pressure fluctuations is clearly visible.

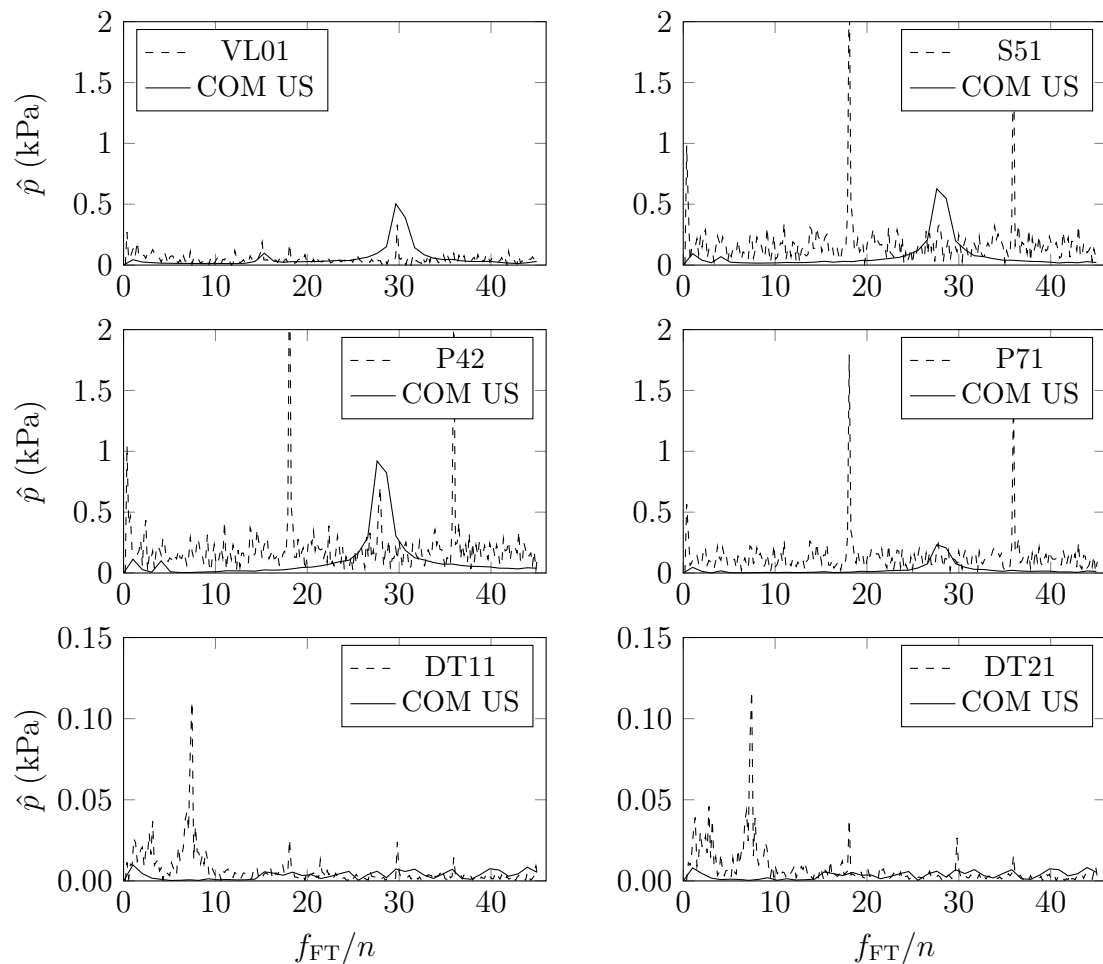


Figure 5.8: FFT of the pressure data at the BEP operating condition

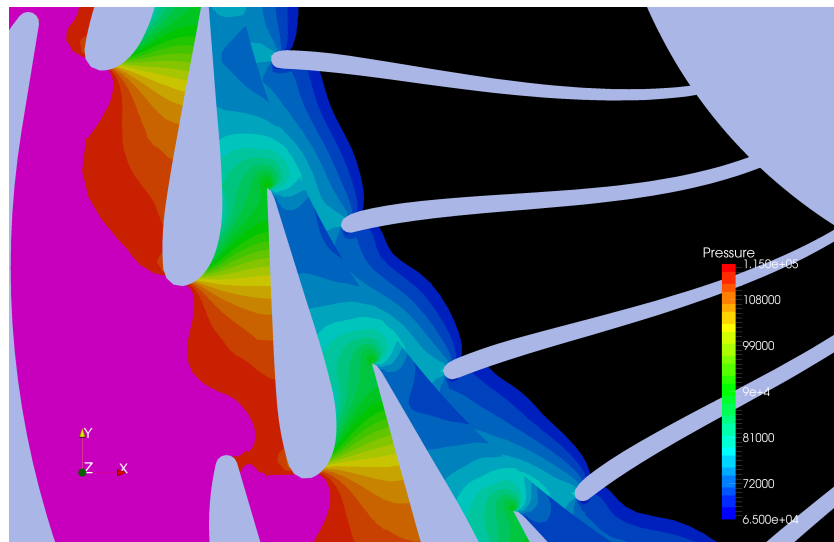


Figure 5.9: Pressure fluctuations at the BEP in the region of the vaneless space

The Fourier transformed pressure fluctuations in the HL condition are shown in figure 5.7. The back-propagation of the passing runner blades is estimated well at the location VL01. The probes at the draft tube location (DT11 and DT21)

reveal no information in the frequency domain. The CFD simulation estimates the influence of the guide vanes on the runner blades, which corresponds to the blade passing frequency. The high peaks at the normalized frequency 19 and 38 correspond to the electric grid frequency of 50Hz. This discrepancy is already pointed out in the discussion of the time series data of the pressure fluctuations. Overall, the simulation results in the HL condition coincide with the results obtained by Buron *et al.* [3], using the Spalart-Almaras turbulence model.

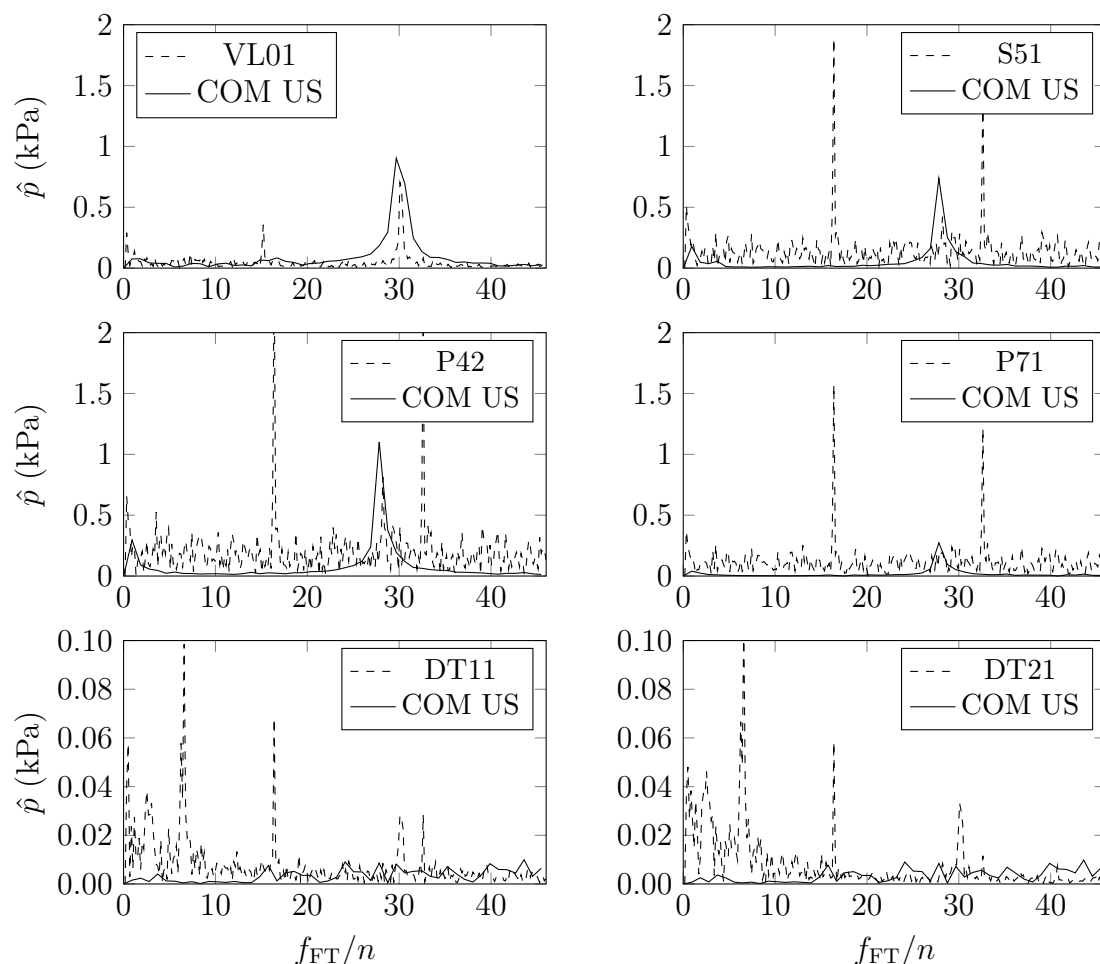


Figure 5.10: FFT of the pressure data at the HL operating condition

Summary pressure fluctuation The pressure probes at the draft tube's wall DT11 and DT21 are insufficiently reproduced by the CFD simulation. In the PL condition the performance is slightly better since the frequency pattern induced by the rotation swirl is estimated. All in all, higher frequency components are not accurately captured. In the vaneless space VL01 the general behavior of the pulsations trend is reproduced in all three operating points. The first characteristic frequency (15) and the second characteristic frequency (30), are estimated in agreement with the experimental data. At the three runner blade locations (S51,

P42 and P71), a highly damped sinusoidal pattern is estimated with a frequency of (28). But in all three operating points, the high pressure spikes occurring in the full length blade with a frequency of 15 are not captured at all.

5.5 Flow energy losses

In this section, the energy losses of the steady-state simulation over the different parts of the turbine are evaluated and compared to the estimations simulated by Jošt *et al.* [6]. The distributor efficiency losses as well as the draft tube losses are investigated at the three operating conditions (PL, BEP and HL). The available power at the Francis turbine model is listed in table 5.5.

Table 5.5: The predicted total available power at the Tokke model Francis turbine

OP	Unit	Power
PL	kW	8.18
BEP	kW	25.68
HL	kW	26.23

5.5.1 Distributor

Table 5.6 compares the losses in the distributor simulated by steady-state and unsteady computations to the work of Jošt *et al.* [6]. Overall, the losses in the HL regime are the lowest. As expected, the highest hydraulic losses occur in the PL condition. Figure 5.11 displays the flow properties around the stay vane and the guide vane in the PL regime. The figure highlights the strong vortex structures in gray, which appear around the stay and the guide vanes. These vortices lead to the severe energy losses.

Table 5.6: Estimated losses in the distributor, steady-state (S) and unsteady (US) CFD simulation using *Commercial code* compared to literature data(*) [6]

OP	Unit	Loss US	Loss S	Loss*
PL	%	7.9	7.5	4.6-6.9
BEP	%	4.3	4.2	4
HL	%	3.2	3.3	3

Furthermore figure 5.11 shows the flow fields in the BEP condition and the HL condition. Both subfigures show very similar flow structures around the blades. The vortex formation on the trailing edge of the guide vane is slightly lower in the HL regime, leading to fewer losses.

Generally, the trend of the estimations for the efficiency losses in the fluid domain are in accordance with literature and the expectations.

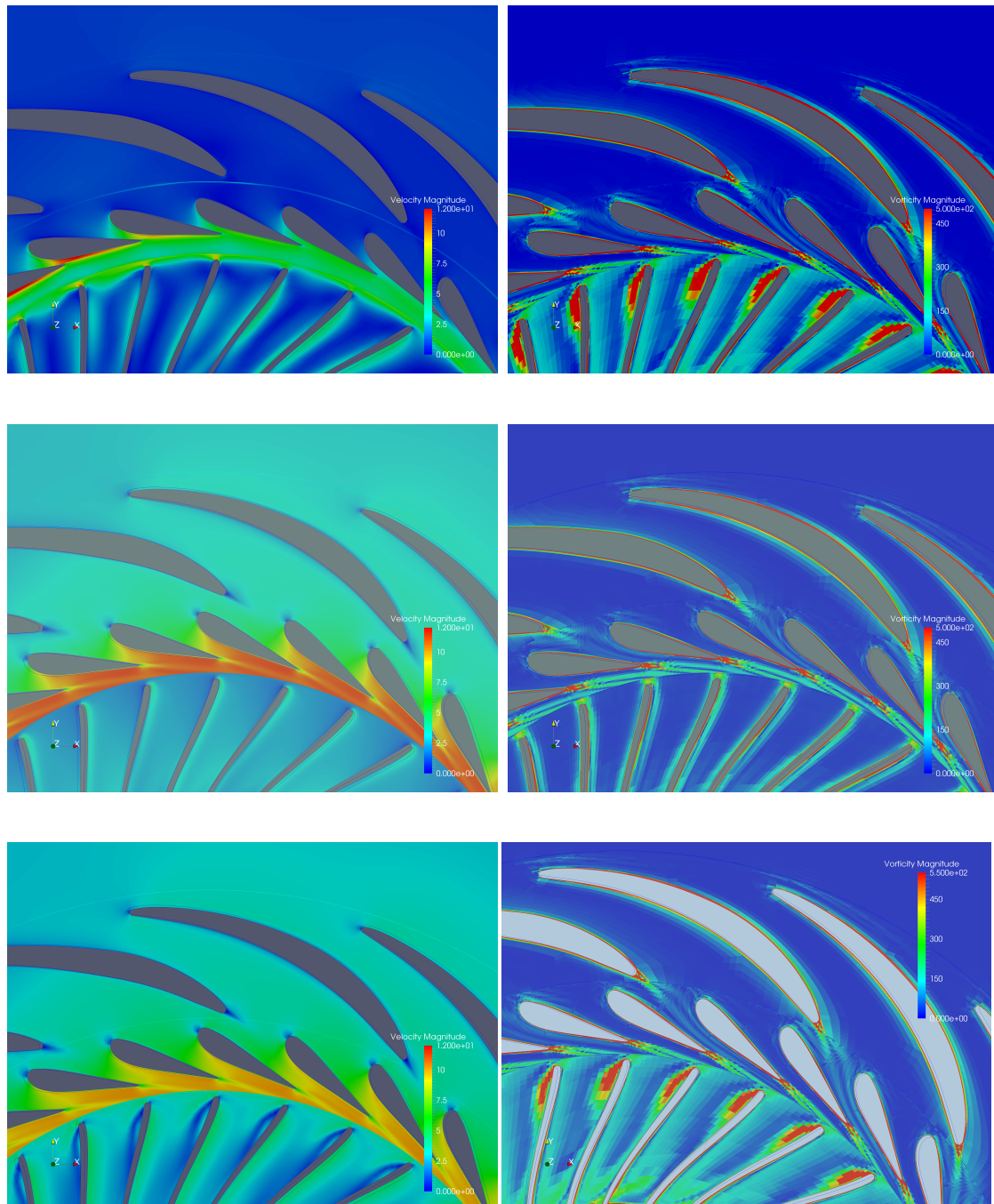


Figure 5.11: Velocity field (left side) and vorticity (right side) in the distributor at PL (top), BEP (middle) and HL (bottom), velocity scale (0 to 12 m/s) and vorticity scale (0 to 500 1/s)

5.5.2 Draft tube

The efficiency losses in the draft tube, estimated by the executed CFD simulation, are presented in table 5.7. The simulation results of the steady-state and unsteady simulation coincide with the literature data [6] in all three operating points.

Table 5.7: Estimated losses in the draft tube, steady-state (S) and unsteady (US) CFD simulation using *Commercial code* compared to literature data(*) [6]

OP	Unit	Loss US	Loss S	Loss*
PL	%	7.5	7.8	6.65-8.9
BEP	%	0.47	0.42	0.46-0.6
HL	%	0.53	0.47	0.56-0.65

In PL the strong vortex formation (figure 5.12) causes intensive power losses in the draft tube. Compared to PL, in the BEP and the HL regime, a small swirl is produced indicating fewer losses. This fact is revealed by looking at the stream lines propagating straight through the draft tube.

Summary efficiency losses Strong vortex structures around the stay and guide vanes cause severe energy losses ($\sim 8\%$) in the distributor at PL. In the BEP and the HL condition fewer hydraulic losses occur ($< 4\%$). The energy loss in BEP is slightly higher than in HL due to the long vortex on the trailing edge of the guide vane. In PL the strong vortex formation causes also high power losses ($\sim 8\%$) in the draft tube. In the BEP and the HL regime, a small swirl is produced indicating fewer losses ($\sim 0.5\%$) in the draft tube. The estimation of the losses coincide with the reference literature [6].

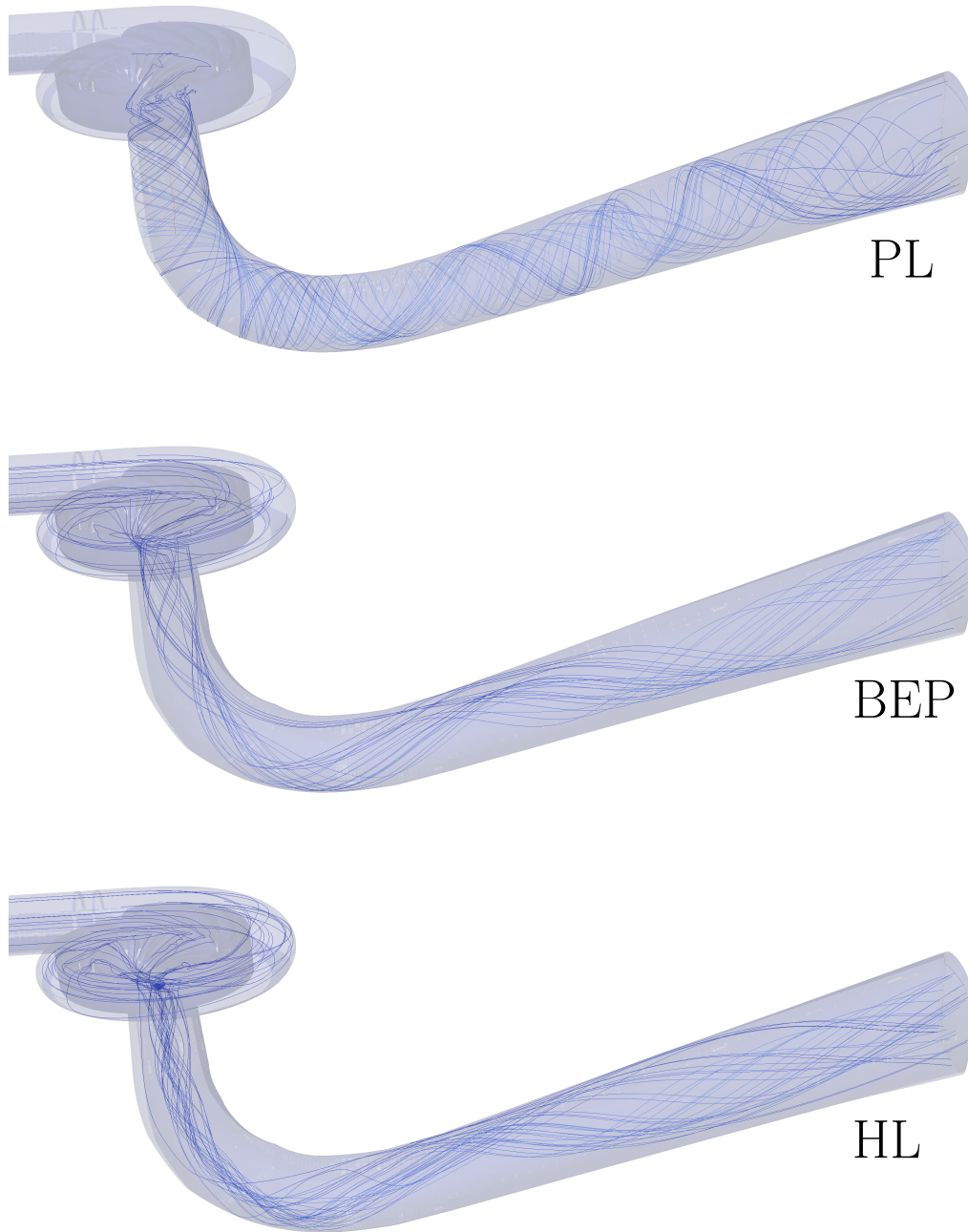


Figure 5.12: Propagating stream line in the draft tube at the three operating conditions

6 Further investigations - Outlook

OpenFoam The simulation in *OpenFOAM* was set up according to the description in the BEP condition. Additional computations may target the other operating conditions and the RSI.

Commercial code As pointed out for *OpenFOAM*, the FFT simulations in *commercial code* are expected to compute more time steps to refine the frequency axis of the FFT graphs.

Additional task 1 Furthermore, as pointed out in the result section, some flow phenomena around the runner draft tube interface are not accurately captured. The investigation of these properties would improve the model's capabilities and the quality of the results.

Additional task 2 The pressure fluctuation plots of the FFT considered the raw measurement data, which is polluted by the grid frequency. A major problem occurs in the PL condition as illustrated in table 6.1. The typical pressure fluctuations interfere with the normalized grid frequency.

Table 6.1: Normalized grid pollution frequencies in the pressure sensor data

OP	Unit	First	Second S	Fourth
PL	–	7.4	14.8	29.6
BEP	–	8.9	18.8	37.6
HL	–	8.2	16.4	32.8

7 Conclusion

This work investigates the turbulent flow in the high head Francis turbine of the Tokke model. The geometry and measurement data of the herein considered scaled down Tokke model, are published on the Francis 99 workshop homepage [1]. Based on this data, steady-state and unsteady flow simulations are set up in *commercial code* and in *OpenFOAM*. In addition to Lenarcic *et al.* [4], further grid refinement and unsteady CFD simulations are considered in this work. The blocking of the components was provided by [4].

The whole domain is meshed in *Ansys ICEM CFD* using a structured grid and structured grid refinement towards the domain interfaces and hydraulic smooth walls. The wall boundary layer is resolved by $y_{mean}^+ \sim 30$ and automatic wall functions. Turbulent flow behavior is modeled by applying the shear stress transport model, $k\omega$ -SST with a medium turbulent intensity at the inlet ($I = 0.05$ and $l_t = 0.01\text{m}$). The three proposed operating conditions are investigated by steady-state and unsteady simulations in *commercial code*. In *OpenFOAM* only the BEP is addressed by an unsteady CFD simulation.

The grid convergence method verifies the ability of monotonic convergence of the medium grid with a wall resolution $y_{mean}^+ \sim 30$. All further computations are based on this grid type meeting computational efficiency and validity of the calculated quantities. The flow domain of the grid convergence study is based on a rationally periodic one passage model. In contrast to the one passage model setup of the grid error estimation, the further simulations are performed on the full turbine model with 5M cells.

The results of the discussed model setups are presented and compared to experimental data. Global quantities, the mean pressure deviations and mean velocity profiles as well as the pressure fluctuations are investigated. Furthermore, the flow properties and the efficiency losses in the distributor and the draft tube are evaluated and compared to literature [6].

Both the unsteady and steady-state simulations, show obvious parallels in their results of the global quantities at the BEP and HL regime. Generally the torque and the net head are overestimated by *commercial code* at these two operating

points. The two global quantities are not captured well, but since they deviate similarly, the estimated hydraulic efficiency is predicted surprisingly well. In PL no obvious trend of the integral quantities is evident, but the deviations are higher compared to the other operating points. The simulation using a finer grid allowed more accurate results compared to the simulation results of Lenarcic *et al.* [4]. The unsteady results behave qualitatively similar to the simulation presented by Trivedi *et al.* [8]. *OpenFoam* is not capable of predicting the hydraulic efficiency compared to the experimental data and *commercial code*.

In the *commercial code* simulation a maximum relative deviation of the static pressure occurs at the location S51 on the suction side of the runner blade. The results are in accordance with the simulation of Nicolle and Cupillard [2], Buron *et al.* [3] as well as Lenarcic *et al.* [4]. The local static pressure data estimated by *OpenFoam* shows a similar tendency as the results of the *commercial code* simulation.

Steady-state and time averaged unsteady mean velocity results are in excellent correlation, indicating no unsteady effects in the draft tube velocity profile. The computed velocity profile coincides with the profiles computed by Lenarcic *et al.* [4] and Aakti *et al.* [5].

The pressure fluctuations at the draft tube's wall DT11 and DT21 are insufficiently reproduced by the CFD simulation. All in all, higher frequency components are not accurately captured. In the vaneless space VL01 the general behavior of the pulsations trend is reproduced in all three operating points.

Strong vortex structures around the stay and guide vanes cause severe energy losses in the distributor at PL. In PL the strong vortex formation causes also high power losses in the draft tube. In the BEP and the HL regime, a small swirl is produced indicating fewer losses in the draft tube. The estimation of the losses coincide with the reference literature [6].

Bibliography

- [1] Ted Karlsson. Workshop francis 99, test case. <http://www.ltu.se/research/subjects/Stromningslara/Konferenser/Francis-99/Test-Case-1.111520?l=en>, 2013. [Online accessed 2014-05-23].
- [2] S Cupillard J Nicolle. Prediction of dynamic blade loading of the francis-99 turbine. *Journal of Physics: Conference Series*, 579(1):012008, 2015.
- [3] R. Lestriez J.D. Buron, S. Houde and C. Deschênes. Application of the non-linear harmonic method to study the rotor-stator interaction in francis-99 test case. *Journal of Physics: Conference Series*, 579(1):012008, 2015.
- [4] M Lenarcic, M Eichhorn, S J Schoder, and Ch Bauer. Numerical investigation of a high head francis turbine under steady operating conditions using foam-extend. *Journal of Physics: Conference Series*, 579(1):012008, 2015.
- [5] E Casartelli G Romanelli L Mangani B Aakti, O Amstutz. On the performance of a high head francis turbine at design and off-design conditions. *Journal of Physics: Conference Series*, 579(1):012008, 2015.
- [6] M Morgut P Mežnar D Jošt, A Škerlavaj and E Nobile. Numerical simulation of flow in a high head francis turbine with prediction of efficiency, rotor stator interaction and vortex structures in the draft tube. 2014.
- [7] Helmut Keck and Mirjam Sick. Thirty years of numerical flow simulation in hydraulic turbomachines. *Acta Mechanica*, 201(1-4):211–229, 2008.
- [8] Chirag Trivedi, Michel J. Cervantes, B. K. Gandhi, and Ole G. Dahlhaug. Experimental and numerical studies for a high head francis turbine at several operating points. *Journal of Fluids Engineering*, 135(11):111102, 2013.
- [9] R. Moritz. Transient cfd-analysis of a high head francis turbine, 2014.
- [10] C. Bauer. *Hydraulische Maschinen und Anlagen I & II*. TU Wien, Institut for energy systems and thermodynamics, 2012.
- [11] J. Giesecke and E. Mosonyi. *Wasserkraftanlagen: Planung, Bau und Betrieb*. Springer Berlin Heidelberg, 2005.

- [12] Alstom. The francis turbine has the widest range of applications among the various types of turbines available. <http://www.alstom.com/products-services/product-catalogue/power-generation/renewable-energy/hydro-power/hydro-turbines/francis-hydro-turbines/>, 2014. [Online accessed 2015-01-27].
- [13] Statkraft. Tokke. <http://www.statkraft.no/Energikilder/vaare-kraftverk/norge/Tokke/>, 2014. [Online accessed 2014-11-11].
- [14] Verbund. Pumpspeicherkraftwerk kaprun-limberg ii. <http://www.verbund.com/pp/de/pumpspeicherkraftwerk/kaprun-limberg2>, 2014. [Online accessed 2014-11-11].
- [15] K. Menny. *Strömungsmaschinen: Hydraulische und thermische Kraft- und Arbeitsmaschinen*. Lehrbuch. Maschinenbau. Vieweg+Teubner Verlag, 2006.
- [16] H. C. Kuhlmann. *Strömungslehre für Wirtschaftsingenieure - Maschinenbau*. TU Wien, 2004.
- [17] H. C. Kuhlmann. *Numerische Methoden der Strömungsmechanik*. TU Wien, 2009.
- [18] D. C. Wilcox. *Turbulence Modeling for CFD*. DCW Industries, Inc., 1993.
- [19] J.H. Ferziger and M. Perić. *Computational Methods for Fluid Dynamics*. Springer London, Limited, 2002.
- [20] H.K. Versteeg and W. Malalasekera. *An Introduction to Computational Fluid Dynamics: The Finite Volume Method*. Pearson Education Limited, 2007.
- [21] B.E. Launder, N.D. Sandham, and Isaac Newton Institute for Mathematical Sciences. *Closure Strategies for Turbulent and Transitional Flows*. Cambridge University Press, 2002.
- [22] Peter. Turbulence intensity. http://http://www.cfd-online.com/Wiki/Turbulence_intensity, 2012. [Online accessed 2014-12-23].
- [23] Binninger B. Simulationstechnik. http://www.itv.rwth-aachen.de/fileadmin/LehreSeminar/Simulationstechnik_I/Unterlagen/AVT-Prozesstechnik/Einf_Simtech.pdf, 2005. [Online accessed 2015-01-27].
- [24] P. J. Roache. Quantification of uncertainty in computational fluid dynamics. *Annual Review of Fluid Mechanics*, 29(1):123–160, 1997.
- [25] Procedure for estimation and reporting of uncertainty due to discretization in cfd applications. *Journal of Fluids Engineering*, 130(7):078001, 2008.

-
- [26] Dmoroian. Turbulence free-stream boundary conditions. http://www.cfd-online.com/Wiki/Turbulence_free-stream_boundary_conditions, 2014. [Online accessed 2014-01-09].
- [27] Håkan Nilsson Lucien Stoessel. Steady and unsteady numerical simulations of the flow in the tokke francis turbine model, at three operating conditions. *Journal of Physics: Conference Series*, 579(1):012008, 2015.

